



1 **Comparison of model and ground observations finds snowpack and blowing snow both contribute**
2 **to Arctic tropospheric reactive bromine**

3 William F. Swanson¹, Chris D. Holmes², William R. Simpson¹, Kaitlyn Confer³, Louis Marelle^{4,5}, Jennie
4 L. Thomas⁴, Lyatt Jaeglé³, Becky Alexander³, Shuting Zhai³, Qianjie Chen⁶, Xuan Wang⁷, Tomás
5 Sherwen^{8,9}

6 ¹Department of Chemistry and Biochemistry and Geophysical Institute, University of Alaska Fairbanks,
7 Fairbanks, Alaska

8 ²Department of Earth, Ocean and Atmospheric Science, Florida State University, Tallahassee, Florida

9 ³Department of Atmospheric Sciences, University of Washington, Seattle, Washington

10 ⁴Institut des Géosciences de l'Environnement (IGE), Institut Polytechnique de Grenoble, Grenoble, France

11 ⁵Laboratoire Atmosphères Observations Spatiales (LATMOS), Sorbonne Université, Paris, France

12 ⁶Department of Civil and Environmental Engineering, Hong Kong Polytechnic University, Hong Kong,
13 China

14 ⁷School of Energy and the Environment, City University of Hong Kong, Hong Kong, China

15 ⁸National Centre for Atmospheric Science, University of York, York, UK.

16 ⁹Department of Chemistry, University of York, York, United Kingdom

17 *Correspondence to:* William F. Swanson (wswanson3@alaska.edu)

18 **Abstract**

19 Reactive halogens play a prominent role in the atmospheric chemistry of the Arctic during
20 springtime. Field measurements and models studies suggest that halogens are emitted to the atmosphere
21 from snowpack and reactions on wind-blown snow. The relative importance of snowpack and blowing
22 snow sources is still debated, both at local scales and regionally throughout the Arctic. To understand
23 implications of these halogen sources on a pan-Arctic scale, we simulate Arctic reactive bromine
24 chemistry in the atmospheric chemical transport model GEOS-Chem. Two mechanisms are included: 1) a
25 blowing snow sea salt aerosol formation mechanism and 2) a snowpack mechanism assuming uniform
26 molecular bromine production from all snow surfaces. We compare simulations including neither
27 mechanism, each mechanism individually, and both mechanisms to examine conditions where one
28 process may dominate or the mechanisms may interact. We compare the models using these mechanisms
29 to observations of bromine monoxide (BrO) derived from multiple-axis differential optical absorption
30 spectroscopy (MAX-DOAS) instruments on O-Buoy platforms on the sea ice and at a coastal site in
31 Utqiagvik, Alaska during spring 2015. Model estimations of hourly and monthly average BrO are
32 improved by assuming a constant yield of 0.1% molecular bromine from all snowpack surfaces on ozone
33 deposition. The blowing snow mechanism increases BrO by providing more surface area for reactive



34 bromine recycling. The snowpack mechanism led to increased BrO across the Arctic Ocean with
35 maximum production in coastal regions, whereas the blowing snow mechanism increases BrO in specific
36 areas due to high surface windspeeds. Our uniform snowpack source has a greater impact on BrO mixing
37 ratios than the blowing snow source. Model results best replicate several features of BrO observations
38 during spring 2015 when using both mechanisms in conjunction, adding evidence that these mechanisms
39 are both active during the Arctic Spring. Extending our transport model throughout the entire year leads
40 to predictions of enhanced fall BrO that are not supported by observations.

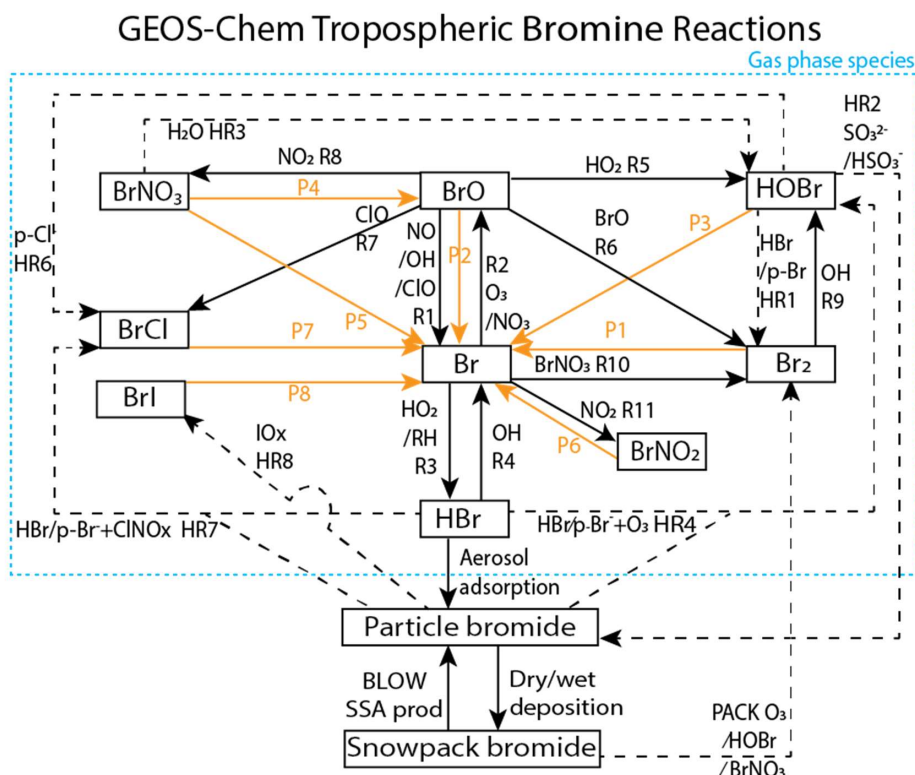
41 1. Introduction

42 Simulating Arctic halogen chemistry is a persistent problem for global models because processes
43 appear to differ between the Arctic and middle latitudes (Parrella et al., 2012; Schmidt et al., 2016).
44 Space-based instruments observe large column densities of reactive bromine across swaths of the Arctic
45 Ocean during the Arctic spring (Chance, 1998; Richter et al., 1998; Wagner and Platt, 1998). Increased
46 levels of tropospheric reactive bromine are associated with ozone depletion events (Barrie et al., 1988;
47 Foster et al., 2001; Koo et al., 2012; Halfacre et al., 2014) as well as oxidation of gaseous elemental
48 mercury (Schroeder et al., 1998; Nghiem, 2013; Moore et al., 2014). Bromine radicals have been
49 observed to lead directly to ozone depletion and mercury oxidation (Wang et al., 2019a). Deposition of
50 oxidized mercury to the snowpack can have deleterious effects on the health of Arctic humans and
51 animals (AMAP, 2011). Arctic reactive bromine chemistry impacts tropospheric oxidative chemistry but
52 is not typically accounted for in global models. Model studies have found that reactive halogen chemistry
53 can explain the oxidation of gaseous elemental mercury (Holmes et al., 2010) and reduce radiative forcing
54 from ozone (Sherwen et al., 2016c). Replicating reactive halogen chemistry in models requires inclusion
55 of multi-phase chemical reactions as well as mechanisms affecting sea salt aerosol particle production and
56 chemical reactions within the snowpack.

57 These increased levels of tropospheric reactive bromine radicals are a product of heterogeneous
58 photochemical reactions at the interface between air and saline surfaces such as surface snowpack and sea
59 salt aerosols (Saiz-Lopez and von Glasow, 2012; Simpson et al., 2015). Figure 1 depicts the gas-phase,
60 heterogeneous, and photochemical reactions thought to control tropospheric bromine, all of which are
61 included in the model and results presented in this manuscript. Bromine radicals (Br) are produced by
62 photolysis of molecular bromine (P1) and react with ozone to form bromine monoxide (BrO) (R2).
63 Under sunlit conditions, BrO is most often photolyzed back to Br radicals and an oxygen atom (P2) that
64 then most often reforms ozone, resulting in a null cycle. Due to this rapid interchange of Br and BrO,
65 these two compounds form the BrO_x family. If processes other than BrO photolysis (P1) convert BrO
66 back to Br without producing ozone, the imbalance between these other processes and P1 result in net



67 ozone depletion. For example, ozone is depleted through R6 or R7 when BrO reacts with another halogen
 68 oxide to form either Br₂ or BrCl, or through other more extended processes. A reactive halogen activating
 69 cycle occurs when a BrO radical reacts with a hydroperoxy (HO₂) radical in R5 to form gaseous
 70 hypobromous acid (HOBr). Heterogeneous chemistry can occur on a saline surface between HOBr and
 71 particulate bromide (p-Br⁻) in HR1 forming Br₂ or particle chloride (p-Cl⁻) in HR6 forming BrCl. For
 72 each cycle of reactions P1, R2, R5, and HR1, one hydroperoxy radical is removed from the atmosphere,
 73 one bromine radical is released to the atmosphere, and one ozone molecule is destroyed. This process of
 74 activation of particulate bromide to Br₂ by consuming other radicals (e.g. HO₂) is known as the "bromine
 75 explosion" (Wennberg, 1999). Ground-based instruments have observed sharp increases in reactive
 76 bromine levels over the course of a single day from below 2 pmol/mol up to a maximum of 41 pmol/mol
 77 (Pöhler et al., 2010). Reactions may also sequester reactive bromine into more stable bromine reservoir
 78 species. BrO may react with nitrogen dioxide (NO₂) in R8 to form bromine nitrate (BrNO₃), which can
 79 also undergo hydrolysis on a saline surface to form HOBr as in HR3.



80

81 **Figure 1: GEOS-Chem tropospheric bromine reactions.** Tropospheric bromine reservoirs shown in
 82 black boxes, with attached lines indicating reactions. Solid black lines R1-R11 indicate gas phase



83 chemical reactions, solid orange lines P1-P8 indicate photolysis reactions, and dashed black lines HR1-
84 HR8 indicate heterogeneous reactions. All gaseous species may undergo wet and dry deposition.
85 Additional sources of tropospheric bromine include the production of particulate bromide by the BLOW
86 mechanisms and the production of Br₂ by the PACK mechanism, as well as the degradation of
87 organobromines to form Br (OR1).

88 A potentially important competitor for recycling of reactive bromine through HOBr is its reaction
89 with sulfur (IV) species, such as the reaction between HSO₃⁻ and HOBr in HR2 (Chen et al., 2017). To
90 the extent that this reaction competes with HR1, it can slow the release of bromide from surfaces and
91 reduce gas-phase reactive bromine (e.g., reduce BrO). Deposition of the HBr formed from HOBr by HR2
92 can remove reactive bromine from the troposphere. In general, the termination of this chemistry leads to
93 formation of HBr, which undergoes gas-particulate uptake to particulate bromide (p-Br⁻).

94 Ozone deposited to a saline surface can oxidize Br⁻ to form HOBr (similar to p-Br⁻ reactions
95 HR4a and HR4b) which is then converted to Br₂ or another dihalogen (e.g., BrCl). Production of reactive
96 bromine during ozone deposition does not require light and can occur at night (Oum et al., 1998; Artiglia
97 et al., 2017). The production of Br₂ is increased at low pH levels (Halfacre et al., 2019).

98 We define the inorganic bromine family, Br_y, in this manuscript as the sum of the bromine
99 species: Br, BrO, HOBr, BrNO₃, 2xBr₂, BrCl, BrI, and HBr, excluding p-Br⁻. The release of bromine from
100 sea salt aerosol particles was found to be the dominant global source of reactive bromine (Sander et al.,
101 2003; Zhu et al., 2019). Sea salt aerosol particles (SSA) sourced from the bursting of bubbles in oceanic
102 whitecaps and other sources and are one of the most abundant aerosol particle types present in the
103 troposphere (De Leeuw et al., 2011). Due to their abundance, SSA particles greatly increase the surface
104 area available for heterogeneous reactive bromine chemistry. Debromination of acidified aerosol
105 increases reactive bromine by 30%, although global models may underestimate Arctic reactive bromine
106 when considering only open ocean-sourced SSA (Schmidt et al., 2016). Initial literature on Arctic reactive
107 bromine chemistry identified aerosol particles as a potential saline surface for reactive bromine
108 photochemistry (Fan and Jacob, 1992; Vogt et al., 1996). If one supposes that SSA can only be produced
109 from the open ocean source of SSA, the lack of Arctic Ocean open water during the winter/spring is at
110 odds with observations of high SSA concentrations observed during the winter months in polar regions
111 (Wagenbach et al., 1998; Huang et al., 2018). The formation of SSA from the sublimation of blowing
112 snow particles over the Arctic Ocean was proposed as an alternate SSA production mechanism (Yang et
113 al., 2008, 2010, 2019). Recent field studies have confirmed the direct production of SSA from blowing
114 snow (Frey et al., 2020). A blowing snow mechanism was implemented in the global chemical model
115 GEOS-Chem and was able to explain wintertime SSA enhancements over the Arctic (Huang and Jaeglé,



116 2017) as well CALIOP-detected aerosol particle abundance (Huang et al., 2018) and high levels of Arctic
117 BrO detected by satellites in spring (Huang et al., 2020).

118 Snowpack containing bromide salts was also identified as a source of reactive bromine (Tang and
119 McConnell, 1996). Molecular bromine was measured above the snowpack at levels up to 25 pmol/mol
120 (Foster et al., 2001). Field experiments demonstrate that the snowpack emits Br₂, Cl₂, and BrCl, with
121 emission affected by ambient ozone levels, the snowpack ratio of bromide to chloride, and exposure to
122 sunlight (Pratt et al., 2013; Custard et al., 2017). Box modeling found that the flux of reactive bromine
123 from the surface of the Arctic Ocean sea ice is a prerequisite for bromine activation (Lehrer et al., 2004).
124 Box modeling found that both HOBr and BrNO₃ can be converted to Br₂ in the snowpack (Wang and
125 Pratt, 2017). Detailed one dimensional models of the snowpack-air interface find that reactive bromine
126 production can occur in the interstitial air between snowpack grains (Thomas et al., 2011; Toyota et al.,
127 2014), with ozone depletion events arising from snowpack reactive bromine production (Thomas et al.,
128 2011; Cao et al., 2016). However, a detailed snowpack model coupled to an atmospheric model would be
129 sensitive to important parameters such as snowpack bromide content and acidity of the air-ice interface
130 that are highly variable across the Arctic (Toom-Sauntry and Barrie, 2002; Krnavek et al., 2012). A
131 mechanism to parameterize the release of molecular bromine from snowpack upon deposition of ozone,
132 HOBr, and BrNO₃ was implemented in the GEM-AQ model and captured many of the observed features
133 of reactive bromine in the Arctic troposphere (Toyota et al., 2011). The mechanisms from Toyota et al.
134 (2011) assumes a 100% yield of molecular bromine on deposition of HOBr or BrNO₃ (see Figure 1
135 PACK) and a diurnally varying yield of Br₂ on ozone deposition of 7.5% during the daytime (solar
136 elevation angle > 5°) and 0.1% during the nighttime (solar elevation angle < 5°) (see Figure 1 PACK). In
137 the Toyota et al. (2011) parameterization, the daytime yield of Br₂ from ozone was increased to 7.5% to
138 match surface ozone depletion observations and is based on the assumption that photochemical reactions
139 in the snowpack would trigger a bromine explosion and amplify the net release of Br₂ (Toyota et al.,
140 2011). Herrmann et al (2021) implemented the Toyota et al. (2011) mechanism in WRF-Chem and found
141 snowpack Br₂ production was capable of replicating ozone depletion events observed in multiple datasets.
142 Marelle et al. (2021) implemented a surface snowpack mechanism based on Toyota et al. (2011) and a
143 blowing snow mechanism based on Yang et al. (2008) and Huang and Jaeglé (2017) and found improved
144 prediction of ozone depletion events, the majority of which were triggered by the snowpack mechanism.
145 The Toyota et al. (2011) mechanism was also implemented in the EMAC model and replicated many of
146 the features of reactive bromine events observed by satellite-based GOME sensor (Falk and Sinnhuber,
147 2018).



148 Field campaigns have directly observed the production of SSA from blowing snow (Frey et al.,
149 2020) as well as production of Br₂ from the snowpack (Pratt et al., 2013) in the environment. This
150 manuscript uses both production mechanisms for the first time in the global chemical model GEOS-
151 Chem. We devised a set of six model runs to test each mechanism individually and together as well as one
152 control run using neither mechanism. We compare BrO simulated in each model run against extensive
153 ground-based observations of BrO made from February to June 2015. This set of modeling scenarios
154 allows identification of the effects of each mechanism on BrO as well as the synergistic effects of both
155 mechanisms working together.

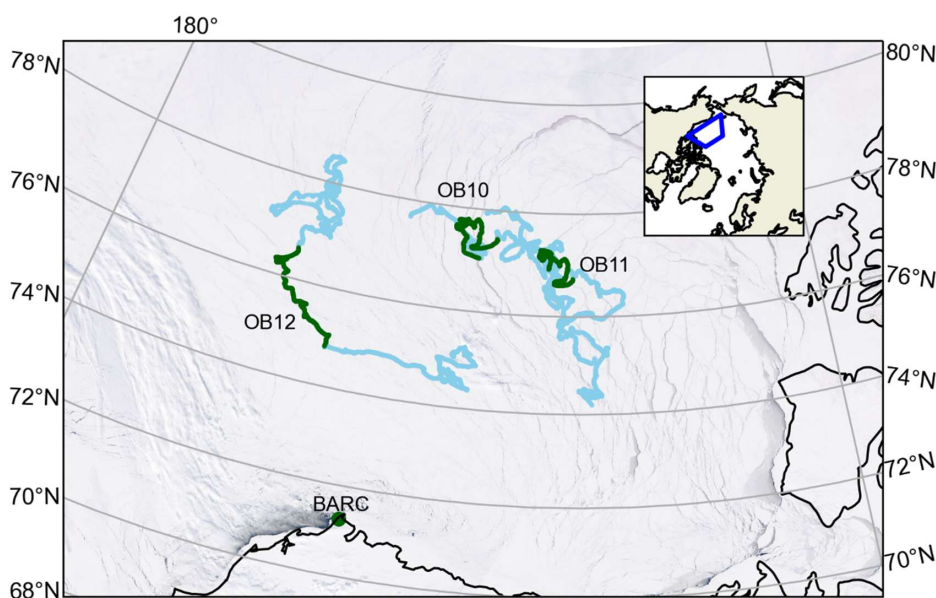
156 2. Data sources and methods

157 2.1 MAX-DOAS observation platforms

158 Multiple axis differential optical absorption spectroscopy (MAX-DOAS) remotely measures the
159 vertical profile of BrO (Hönninger and Platt, 2002; Carlson et al., 2010; Frieß et al., 2011; Peterson et al.,
160 2015; Simpson et al., 2017). BrO is commonly used as a proxy for total tropospheric reactive bromine
161 (Chance, 1998; Richter et al., 1998; Wagner and Platt, 1998; Theys et al., 2011; Choi et al., 2012). MAX-
162 DOAS instruments were mounted on all of the fifteen floating autonomous platforms (O-Buoys) deployed
163 in the Arctic sea ice as a part of the National Science Foundation-funded Arctic Observing Network
164 project (Knepp et al., 2010). Since MAX-DOAS requires sunlight to operate, measurements are not
165 available in winter. Spring observations on the O-Buoys typically begin in April when there is enough O-
166 Buoy solar power to defrost the MAX-DOAS viewport. Figure 2 shows the O-Buoys active during 2015.
167 O-Buoy 10 was deployed into sea ice in fall 2013 and measured reactive halogen chemistry in spring
168 2014 and 2015. Most O-Buoys were destroyed in the summer, crushed between fragments of melting sea
169 ice. However, O-Buoy 10 survived summer 2014 in an intact ice floe, survived the winter of 2014-15,
170 and re-started MAX-DOAS observations in April 2015. O-Buoys 11 and 12 were deployed in fall 2014
171 and also re-started observing BrO in April 2015. Figure 2 shows the GPS-derived tracks of the O-Buoys
172 for their full deployment and highlights the O-Buoy locations from April to June 2015 when the BrO
173 observations considered in this analysis were gathered. A MAX-DOAS instrument of the same design
174 was deployed at the Barrow Arctic Research Center (BARC) on the coast of the Arctic Ocean located at
175 156.6679°W, 71.3249°N near Utqiagvik, AK (Simpson, 2018), also shown in Figure 2. Unlike the O-
176 Buoy MAX-DOAS systems, which were powered by batteries and solar panels, the BARC MAX-DOAS
177 was powered from local utilities and was able to defrost its viewport to gather BrO observations earlier in
178 the year, including February and March 2015. The BARC MAX-DOAS data was compared with two O-
179 Buoy style MAX-DOAS instruments deployed on Icelander platforms (deployed on top of sea ice instead
180 of within) and measurements from the various MAX-DOAS systems were found to be comparable
181 (Simpson et al., 2017). The reactive bromine season ends when the BrO slant column densities fall below



182 the instrument detection limit and do not recover, which we call the seasonal end date (Burd et al., 2017).
183 All O-Buoy and BARC (Utqiagvik) data are available at arcticdata.io (Simpson et al., 2009) (Simpson,
184 2018). More information on the time periods of spring BrO observations can be found in Swanson et al.
185 (2020) and Burd et al. (2017). For comparison to the MAX-DOAS BrO observations, GEOS-Chem model
186 simulations are sampled along the GPS-derived paths of O-Buoys 10, 11 and 12 as well as at BARC.



187

188 **Figure 2: Locations of MAX-DOAS BrO observations used in this work.**

189 Blue lines show the drift tracks of O-Buoys, with green showing the locations with valid BrO
190 measurements in spring 2015. Location of Barrow Arctic Research Center (BARC) in Utqiagvik indicated
191 by green dot. Inset map shows True color MODIS imagery on 1 April 2015 shows typical sea ice
192 coverage (NASA 2015).



193 2.2 MAX-DOAS profile retrieval

194 Vertical profiles of BrO were derived from MAX-DOAS observations by means of optimal
195 estimation inversion procedures detailed in Peterson et al. (2015) with settings detailed in Simpson et al.
196 (2017). The HeiPro optimal estimation algorithm (Frieß et al., 2006, 2019) is used to retrieve a vertical
197 profiles of BrO between the surface and 4km from the MAX-DOAS observations. Examination of the
198 averaging kernels from each MAX-DOAS retrieval finds the retrieved vertical profile of BrO is best
199 represented by two quantities: the vertical column density of BrO in the lowest 200 m, and the vertical
200 column density of BrO in the lowest 2000 m of the troposphere referred to in this manuscript as $\text{BrO}_{\text{LTcol}}$
201 (Peterson et al., 2015). We approximate surface mixing ratio by assuming well mixed constant
202 distribution of BrO throughout the lowest 200 m. This mixing ratio is reported as $\text{BrO}_{\text{pptv200}}$ (Simpson et al
203 2009, Simpson 2018). It was shown in Peterson et al. (2015) that these two quantities were largely
204 independent of each other, were fairly insensitive to variations in the assumed prior profile, and
205 represented the ~2-3 degrees of freedom for signal indicated by the optimal estimation retrieval. An
206 important consideration of this method is that when the visibility is poor, the MAX-DOAS is unable to
207 traverse the lowest 2000m AGL and the $\text{BrO}_{\text{LTcol}}$ cannot be measured accurately. Therefore, our quality-
208 control algorithm eliminates $\text{BrO}_{\text{LTcol}}$ observations when the degrees of freedom for signal in the lofted
209 (200m - 2000m AGL) layer were below 0.5 (Simpson et al., 2017). The average fitting error (1σ error) of
210 $\text{BrO}_{\text{LTcol}}$ during spring 2015 was 5.6×10^{12} molecules/cm².

211 2.3 SSA production from open ocean

212 Seafoam from breaking waves and bursting of bubbles forms aerosol droplets suspended in the
213 marine boundary layer (Lewis and Schwartz, 2004). We calculate emission of sea salt aerosol particles
214 from the open ocean as a function of wind speed and sea surface temperature (SST) using the mechanism
215 initially described in Jaeglé et al. (2011) and updated with decreased emissions over cold ($\text{SST} < 5^\circ\text{C}$)
216 ocean waters (Huang and Jaeglé, 2017). Two separate SSA tracers are transported: accumulation mode
217 SSA ($r_{\text{dry}} = 0.01\text{--}0.5 \mu\text{m}$) and coarse mode SSA ($r_{\text{dry}} = 0.5\text{--}8 \mu\text{m}$). Sea salt bromide is emitted assuming
218 bromine content of 2.11×10^{-3} kg Br per kg of dry SSA (primarily NaCl) based on the mean ionic
219 composition of sea water (Sander et al., 2003). Bromide content is tracked separately on accumulation
220 mode SSA and on coarse mode SSA. Heterogeneous chemical reactions can convert SSA-transported
221 bromide into gaseous reactive bromine species in the atmosphere. We run our open ocean SSA
222 calculations at 0.5° latitude x 0.625° longitude spatial resolution using the harmonized emissions
223 component (HEMCO) for highest possible detail (Keller et al., 2014; Lin et al., 2021) including cold
224 water corrections used in Jaeglé et al. (2011). Production of SSA from open oceans which can lead to
225 Arctic reactive bromine recycling on advected open ocean SSA within GEOS-Chem. Each of our model



226 runs reads the dataset generated offline by HEMCO rather than spend computational time replicating
227 open ocean SSA emissions. We call our control run using only open ocean SSA emissions BASE.

228 **2.4 Blowing snow SSA production**

229 Snow can be lofted from the snowpack into the lowest layers of the troposphere by high
230 windspeeds, where it can undergo saltation (bouncing leading to fragmentation) and sublimation to form
231 SSA (Yang et al., 2008, 2010; Frey et al., 2020). This process is modeled as a function of humidity,
232 ambient temperature, windspeed, and the salinity of the blowing snow (Yang et al., 2008, 2010). Three
233 thresholds must be met for SSA production from blowing snow (Dery and Yau, 1999; Déry and Yau,
234 2001). A temperature threshold restricts SSA production from blowing snow to temperatures below
235 freezing. The humidity threshold is based on relative humidity with respect to ice. Sublimation from snow
236 crystals cannot occur if the air is saturated, and no SSA is produced if RH_{ice} is greater than 100%. The
237 windspeed threshold requires ten-meter wind speed to be greater than a threshold value defined in
238 Equation 1 for any production of SSA (Dery and Yau, 1999; Déry and Yau, 2001).

$$239 \quad U_t = 6.975 + 0.0033(T_s + 27.27)^2 \quad (1)$$

240 The wind speed threshold (U_t) is dependent on surface temperature (T_s) in Celsius with a minimum
241 threshold of 6.975 m/s at -27.27 C° and a maximum threshold at 0 C° of 9.429 m/s. The ten-meter
242 windspeed threshold is the most stringent and often controls the production of SSA from blowing snow.

243 Production of blowing snow and SSA is highly sensitive to surface windspeed. We use the
244 highest resolution surface windspeed dataset to ensure the most accurate modeling of SSA and reactive
245 bromine. The MERRA-2 Global Reanalysis Product has a 0.5° latitude x 0.625° longitude resolution
246 which is typically re-gridded to a lower resolution for global chemical modeling. Previous use of the
247 snowpack blowing snow mechanism has simulated blowing snow with MERRA-2 data re-gridded to
248 either $2^\circ \times 2.5^\circ$ or $4^\circ \times 5^\circ$ latitude and longitude (Huang and Jaeglé, 2017; Huang et al., 2018, 2020). Re-
249 gridding to coarser spatial resolution may smooth out the highest ten-meter windspeeds by averaging
250 them with lower windspeeds in the grid cell. The Utqiagvik MERRA-2 ten-meter windspeeds at different
251 spatial resolutions are shown in Supplemental Figures S1, S2 and S3 to illustrate this effect. Average
252 Utqiagvik ten-meter windspeeds for 2015 are 5.3 m/s at $2^\circ \times 2.5^\circ$ resolution and 5.5 m/s at $0.5^\circ \times 0.625^\circ$
253 resolution. The maximum Utqiagvik ten meter windspeed at MERRA-2 2×2.5 is 16.3 m/s, while the
254 maximum windspeed at MERRA-2 $0.5^\circ \times 0.625^\circ$ is 19.3 m/s. These extremely high windspeed events are
255 more common at higher spatial resolution and can contribute an outsized amount of SSA to the marine
256 boundary layer. Supplemental Figure S4 shows the measured ten-meter windspeed at BARC, along with
257 daily average threshold windspeed (Equation 1). Spikes in daily averaged windspeed at BARC in April
258 can contribute to SSA formation and justify the use of high-resolution MERRA-2 wind speed data.



259 Snow salinity is influenced by snow age and the material underlying the snow (Krnavek et al.,
260 2012). The median surface snowpack salinity near Utqiagvik was measured at 0.67 practical salinity units
261 (PSU)PSU for 2-3 weeks old sea ice, 0.12 PSU for thicker first year ice, and 0.01 PSU for multi-year ice
262 (MYI) (Krnavek et al., 2012). Snow salinity is also a function of snow depth above sea ice, with blowing
263 surface snow having much lower salinity than snow at depth that is in contact with the sea ice (Frey et al.,
264 2020). Domine et al. (2004) measured median salinity at 0.1 PSU on snowpack over first year ice and
265 0.02 PSU on snowpack over multi-year ice. In this analysis we use a salinity of 0.1 PSU on first-year sea
266 ice as in Huang et al. (2020). The production of reactive bromine from sea ice types is entirely dependent
267 on PSU in this parameterization. Previous modeling efforts have used 0.01 PSU for MYI (Huang et al.,
268 2018) and underestimate BrO production in high Arctic areas with increased MYI coverage. The bromide
269 content of surface snow over MYI is enriched by deposition of SSA and trace gases, and MYI regions
270 may play a role in springtime halogen chemistry (Peterson et al., 2019). Previous analysis of O-Buoy data
271 found no statistically significant differences in springtime BrO between regions of the Arctic (Swanson et
272 al., 2020). We use 0.05 PSU for snowpack on MYI as in Huang et al. (2020).

273 Another important parameter for SSA formation is the number of SSA particles formed from each
274 blowing snowflake. A value of 5 particles per snowflake was used in Huang and Jaeglé (2017) based on
275 wintertime observations of supermicron and sub-micron SSA at Barrow. Values of 1 and 20 particles per
276 snowflake have been tested (Yang et al., 2019) but it is unclear which value was more realistic. We use a
277 particle formation value of 5 particles per snow grain as in Huang et al. (2020).

278 Snowpack may be enriched or depleted in bromide compared to seawater, which is thought to be
279 an effect of atmospheric deposition or release of bromine from snowpack (Krnavek et al., 2012).
280 Snowpack enrichment due to atmospheric deposition is less pronounced when snowpack salinity is high,
281 with snowpack containing $1000 \mu\text{M Na}^+$ (approximately 0.06 PSU) or more never exceeding twice the
282 seawater ratio of bromine to chloride (Krnavek et al., 2012). Domine et al. (2004) found an increased
283 enrichment factor of five times seawater in snow with a salinity of $100 \mu\text{M Cl}^-$ (approximately 0.006
284 PSU). We use a snowpack enrichment factor of bromide five times that of seawater as in Huang et al.
285 (2020) where this enrichment best agreed with GOME-2 observations. However, we note that a bromide
286 enrichment factors five times seawater exceeds enrichment factors of two measured in snowpack with a
287 salinity of 0.1 PSU (Krnavek et al., 2012).

288 Our choice of model input settings is similar to Huang et al. (2020) but we will be running the
289 blowing snow mechanism in HEMCO at a 0.5° latitude \times 0.625° longitude spatial resolution. The model
290 run using the results of our high-resolution blowing snow SSA HEMCO simulation is called BLOW.



291 **2.5 Snowpack emissions of molecular bromine**

292 We base our Br₂ emissions scheme on Toyota et al. (2011) and Marelle et al. (2021), which
293 prescribe a yield of Br₂ upon snowpack deposition of ozone, BrNO₃ and HOBr. In other modeling studies,
294 this simplified deposition-based mechanism captured the synoptic-scale behavior of reactive bromine
295 production across the Arctic (Toyota et al., 2011; Falk and Sinnhuber, 2018; Herrmann et al., 2021;
296 Marelle et al., 2021). These modeling studies used different yields of Br₂ upon deposition over land
297 snowpack, multi-year ice, and first year ice, restricting the production of molecular bromine from ozone
298 deposition to first year ice surfaces. None of these studies were coupled to a snowpack model tracking
299 snow bromide, and effectively assume an infinite bromide reservoir with Br₂ production limited only by
300 the deposition flux and Br₂ yield.

301 Field studies indicate that snowpack over multi-year ice, first-year ice, and land regions may
302 contribute to reactive bromine chemistry. Krnavek et al. (2012) found snow bromide content spanning six
303 orders of magnitude, with individual samples taken from multi-year ice, first-year ice, and land regions
304 showing variability of up to three orders of magnitude for each region. Analysis of variance in
305 tropospheric BrO from 2011-2016 found no statistically significant differences in tropospheric BrO
306 between different regions of the Arctic (Swanson et al., 2020). Both coastal snowpack and multi-year ice
307 regions may produce reactive bromine. Molecular bromine production has been observed from coastal
308 snowpack on exposure to ozone (Pratt et al., 2013; Custard et al., 2017). Airborne sampling has observed
309 enhanced BrO up to 200 km inland (Peterson et al., 2018). Snow above multi-year sea ice regions is
310 depleted in bromide, indicating that it may play a role in Arctic bromine chemistry (Peterson et al., 2019).

311 Our modeling study tests the hypothesis that all snow has a uniform ability to produce molecular
312 bromine, effectively assuming an infinite bromide reservoir with Br₂ production limited only by the
313 deposition flux. We differ from previous model parameterizations in allowing uniform Br₂ production
314 upon snowpack deposition of ozone, BrNO₃ and HOBr over all sea ice surfaces and selected coastal
315 snowpack regions. We expect higher predictions of snowpack molecular bromine production than recent
316 modeling efforts (Herrmann et al., 2021; Marelle et al., 2021) in which ozone deposition over land and
317 multi-year ice surfaces did not produce molecular bromine.

318 **2.5.1 Snowpack Br₂ production over sea ice**

319 We assume a uniform production of Br₂ on deposition to snowpack over oceanic ice whether the
320 ice is first-year sea or multi-year sea ice. We use MERRA-2 fractional ocean ice coverage fields, which
321 introduces some artifacts. MERRA-2 classifies the freshwater Great Lakes as ocean, but sea ice and
322 snowpack on those frozen lakes is unlikely to have sufficient bromide to support large Br₂ fluxes due to
323 its distance from the ocean. Therefore, we specifically prohibit snowpack Br₂ emissions in the Great



324 Lakes region (between 41° N and 49° N latitude and 75° W and 93° W longitude). This choice is in
325 agreement with McNamara et al. (2020), who found road salt derived aerosol particles are responsible for
326 80-100% of atmospheric ClNO₂ in Michigan with no mention of a source of reactive halogens from
327 nearby Great Lakes.

328 **2.5.2 Snowpack Br₂ production over land**

329 We wish to only enable production of Br₂ over land if the snowpack is sufficiently enriched in
330 bromide. Snowpack over land surfaces and glaciers may be enriched in bromide by oceanic SSA sources
331 (Jacobi et al., 2012, 2019). The distance that SSA may be transported inland from the coast is limited by
332 geographical features such as mountains. Based on direct observations of reactive bromine chemistry up
333 to 200 km from the Alaskan coastline (Peterson et al., 2018), we include unlimited production of Br₂ from
334 specific land grid cells within 200 km of the coast upon deposition of ozone, HOBr, and BrNO₃. We only
335 allow the fraction of each grid cell that is within 200 km of the coastline (Group and Stumpf, 2021) to
336 produce molecular bromine. We further restrict snowpack Br₂ emissions to locations that are less than 500
337 m above sea level, because higher elevation locations are unlikely to be enriched by sea spray. This
338 altitude screen eliminates Br₂ emissions from coastal mountains such as the Alaskan Rockies, the Brooks
339 Range in Alaska, and the Scandinavian Mountains as well as from the Greenland Plateau. Halogen
340 chemistry may occur over the Greenland ice sheet (Stutz et al., 2011) contrary to this screen, but this will
341 have minimal impact on the regions of interest in this manuscript.

342 Our final screen is based on the average snow depth in each land grid cell. Both modeling studies
343 (Thomas et al., 2011; Toyota et al., 2014) and field studies (Domine et al., 2004; Pratt et al., 2013;
344 Custard et al., 2017; Frey et al., 2020) agree that bromine chemistry can occur in the better ventilated and
345 illuminated top of the snowpack. Regions with less than 10 cm of snowpack may not have sufficient
346 snow for reactive bromine chemistry, thus we only produce snowpack Br₂ when the average snow depth
347 in a land grid cell is 10 cm or greater. This screen prevents molecular bromine production in the lower
348 latitude regions with minimal snow coverage and is necessary because ozone deposition to plants in
349 snow-free grid cells often exceeds the slow deposition of ozone to snowpack and would not be expected
350 to produce Br₂.

351 **2.5.3 Diurnal yield of Br₂ on ozone deposition**

352 We choose two alternate assumptions for the yield of Br₂ during the day. Toyota et al. (2011)
353 initially assumed a constant yield of Br₂ from ozone deposition of 0.1% based on laboratory observations
354 of nighttime bromine activation on ozone deposition (Oum et al., 1998; Wren et al., 2010, 2013) and then
355 adjusted the daytime yield of Br₂ on ozone deposition to 7.5% to better match surface ozone mixing ratios
356 measured at coastal stations. This increased daytime yield value was chosen based on the assumption that



357 photochemistry may trigger an autocatalytic cycle leading to a 75-fold increase in Br₂ yield. The
358 PHOTOPACK runs uses the increased daytime Br₂ yield of 7.5% when the solar elevation angle is 5° or
359 greater. Previous implementations of the snowpack mechanism (Toyota et al., 2011; Herrmann et al.,
360 2021; Marelle et al., 2021) predict ozone deposition velocities over Arctic sea ice on the order of 0.01
361 cm/s. Our model predicts similar ozone deposition rates over polar open ocean of 0.009 cm/s (Pound et
362 al., 2020), but our model currently predicts deposition velocities over Arctic sea ice between 0.02 cm/s
363 and 0.1 cm/s based on the month (see Supplemental Figure S5), with higher values influenced by
364 proximity to the coast as described in Bariteau et al. (2010).. Thus, our PHOTOPACK run may predict
365 much higher Br emissions than previous snowpack predictions despite the same yield values due to
366 differences in deposition. To match out magnitude of Br₂ production with previous implementations of
367 the snowpack mechanism (Toyota et al., 2011; Herrmann et al., 2021; Marelle et al., 2021) we add two
368 PACK runs with a constant Br₂ yield on ozone deposition of 0.1% based on yield values in Toyota et al.
369 (2011). Both PACK and PHOTOPACK runs assume 100% conversion of deposited HOBr and BrNO₃ to
370 Br₂. Table 1 shows further model run yield details.

371 **Table 1 Model run settings**

372 Sea salt aerosol particles are produced from blowing snow as detailed in Section 2.5. Daytime is defined
373 as when the solar elevation angle is greater than 5°, nighttime is defined as when the solar elevation angle
374 is less than 5°.

Model Run	Blowing snow SSA produced	Millimoles Br yielded per mole O ₃ deposited (daytime)	Millimoles Br yielded per mole O ₃ deposited (nighttime)
BASE	FALSE	0	0
BLOW	TRUE	0	0
PACK	FALSE	1	1
BLOW+PACK	TRUE	1	1
PHOTOPACK	FALSE	75	1
BLOW+PHOTOPACK	TRUE	75	1

375

376 **2.6 GEOS-Chem chemistry and transport model**

377 The GEOS-Chem global atmospheric chemistry and transport model (Bey et al., 2001) simulates
378 emissions, transport, and chemistry of atmospheric trace gases and aerosols, including halogens. The
379 chemical mechanism in GEOS-Chem 12.9.3 (<http://www.geos-chem.org>, last access 29 October 2019,
380 DOI:10.5281/zenodo.3974569) includes HO_x-NO_x-VOC-O₃-halogen-aerosol tropospheric chemistry
381 (Mao et al., 2013; Fischer et al., 2014; Fisher et al., 2016; Travis et al., 2016; Wang et al., 2021). The
382 model has been regularly and consistently updated to reflect current understanding of heterogeneous and
383 gas-phase halogen chemistry.



384 Halogens in the troposphere may be sourced from photooxidation of halocarbons, emissions of
385 iodine from the ocean surface, downward transport of halogens from the stratosphere, and release of
386 halogens through heterogeneous chemistry on SSA. Figure 1 shows a simplified version of the GEOS-
387 Chem reaction scheme focusing on tropospheric bromine reactions and reservoirs. Heterogeneous
388 reactions for release of reactive bromine from aerosol surfaces were added to GEOS-Chem (Parrella et
389 al., 2012) and have been updated to include multiphase reactions and reactions between bromine, chlorine
390 and iodine species (Schmidt et al., 2016; Sherwen et al., 2016a; Wang et al., 2019b) as well as input from
391 the stratosphere (Eastham et al., 2014). Recent updates also include reactions between sulfur (IV) species
392 and HOBr, which lead to a 50% decrease in Br_y due to the scavenging of HOBr on aerosol surfaces
393 containing sulfur (Chen et al., 2017). These HOBr-sulfur(IV) reactions are critical in moderating
394 tropospheric BrO in the mid latitudes (Zhu et al., 2019). In GEOS-Chem 12.9 the halogen chemical
395 mechanism was modified extensively to include chlorine chemistry as detailed in Wang et al. (2019b)
396 with update halogen-sulfur (IV) rates (Liu et al., 2021) as well as improved cloud pH calculation from
397 Shah et al. (2020). For the simulations here, GEOS-Chem uses the Modern-Era Retrospective Analysis
398 for Research and Applications, version 2 (MERRA-2) assimilated meteorological fields (Gelaro et al.,
399 2017) re-gridded from native resolution of 0.5°x0.625° latitude and longitude to 2°x2.5° using a reduced
400 vertical grid of 47 layers.

401 We initialize our model in October 2014 from a full-chemistry benchmark file, allowing for 6
402 months of spinup before our period of interest spanning from March to November 2015. We run six
403 different model simulations with settings detailed in Table 1. The base model (BASE) includes the
404 halogen sources described above but no Arctic-specific halogen sources. The BLOW simulation adds
405 SSA production from blowing snow following Huang et al (2020) but using a more recent version of
406 GEOS-Chem. The PACK simulation adds snowpack Br₂ emissions using a constant yield from O₃
407 deposition. The PHOTOPACK simulation also emits Br₂ from snowpack but increases the Br₂ yield from
408 O₃ deposition under sunlight. These blowing snow and snowpack sources are combined in the
409 BLOW+PACK and BLOW+PHOTOPACK simulations.

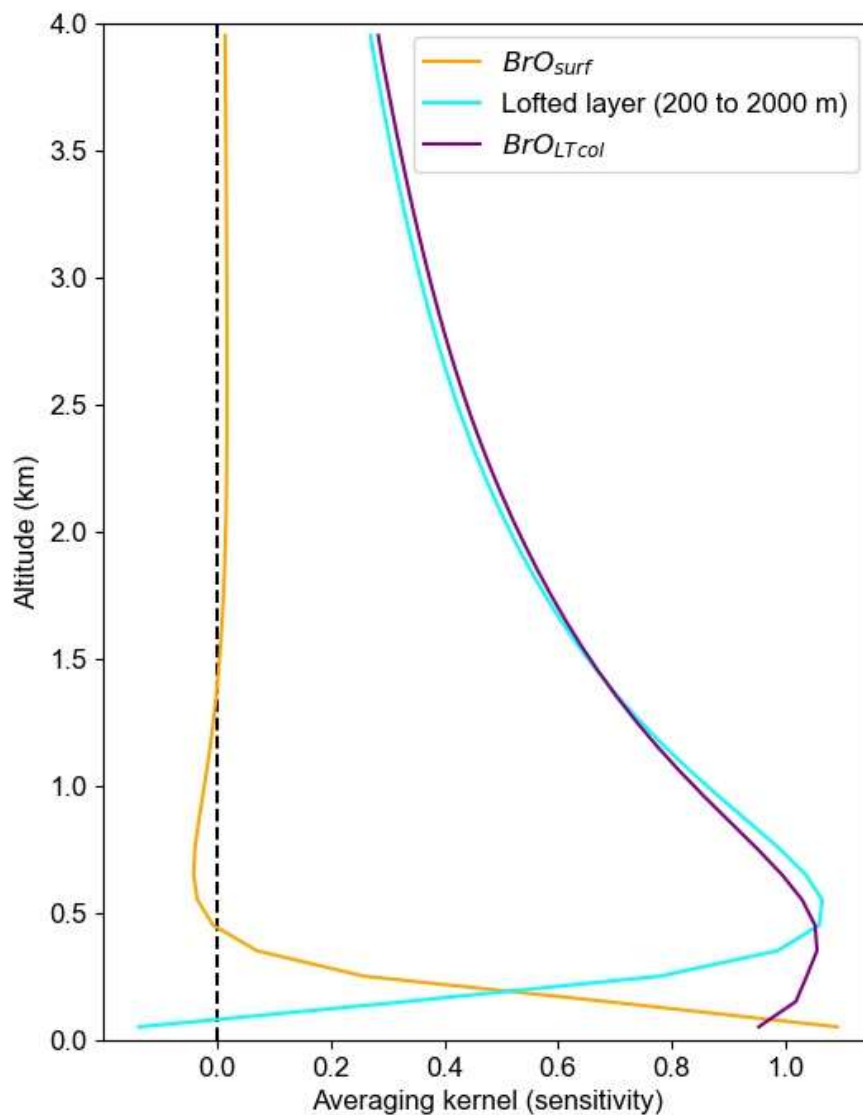
410 **2.7 Comparing GEOS-Chem results to MAX-DOAS vertical column densities**

411 GEOS-Chem simulates BrO mixing ratios for each of its 47 atmospheric layers. Reducing the
412 vertical resolution of the more-resolved GEOS-Chem predictions to be comparable to the coarser MAX-
413 DOAS data is necessary for appropriate comparison (Rodgers and Connor, 2003). To compare the
414 GEOS-Chem profiles with these two grid-coarsened quantities, we grid-coarsen the averaging kernels
415 produced by the HeiPro retrieval algorithm using Supplemental Equation S1 from Payne et al. (2009) to
416 the partial column averaging kernels shown in Figure 3. We use the average of all April averaging kernels



417 that pass our quality criteria (>0.5 DOFS in the lofted layer), which generally represents non-cloudy
418 conditions. We calculate modeled $\text{BrO}_{\text{LTcol}}$ by applying the partial column averaging kernels shown in
419 Figure 3 to the GEOS-Chem modeled vertical BrO profiles.

420 Figure 3 shows the average partial column averaging kernel for the surface layer (0-200m AGL)
421 has near unit sensitivity to BrO at the ground, decaying to about 0.5 at 200m AGL then to zero at about
422 400m AGL, as desired. The sensitivity of the $\text{BrO}_{\text{LTcol}}$ is near unity from about the surface to 600m AGL,
423 then slowly decays with 0.5 sensitivity at 2000m AGL. The resulting sensitivity to mid-tropospheric BrO
424 means that free-tropospheric BrO produced by the GEOS-Chem model contributes to modeled $\text{BrO}_{\text{LTcol}}$,
425 albeit at 50% or lower sensitivity, even if the GEOS-Chem-predicted free-tropospheric BrO is above the
426 nominal 2000m top of the integration window. The residual sensitivity of the $\text{BrO}_{\text{LTcol}}$ averaging kernel
427 above 2000m is caused by the limited ability of ground-based MAX-DOAS to distinguish the true altitude
428 of BrO at non-tangent geometries (higher viewing elevation angles) that are required to view BrO at these
429 higher altitudes. Figure 3 shows that BrO above 4 km makes only a small contribution to the modeled
430 $\text{BrO}_{\text{LTcol}}$, which was not included in the $\text{BrO}_{\text{LTcol}}$.



431

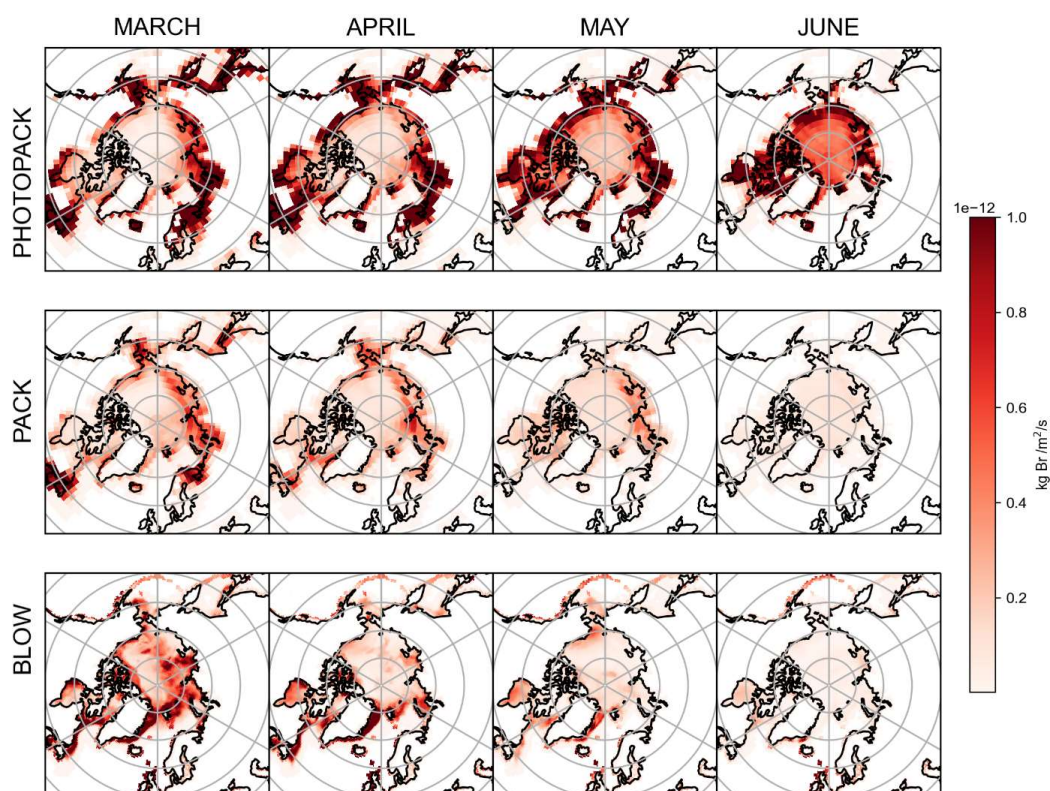
432 **Figure 3: Averaging kernels showing the sensitivity of retrieved $\text{BrO}_{\text{LTcol}}$ and retrieved BrO_{surf} to**
433 **BrO at a range of altitudes.**

434 Each line represents a row of the averaging kernel matrix. BrO_{surf} is the column from the surface to 200 m
435 and $\text{BrO}_{\text{LTcol}}$ is the column up to 2000 m.

436 Although it has been suggested in the literature (von Clarmann and Glatthor, 2019) that averaged
437 averaging kernels can cause problems, we do not report data when there are clouds and thus are only
438 using the more consistent averaging kernels that occur under clear sky conditions. We use other criteria
439 related to vertical visibility to identify clear skies. As described in Peterson et al. (2015), the information



440 content (DOFS) in the lofted layer is nearly linearly related to the aerosol optical depth. We find that the
441 slant column density of the O₂-O₂ collisional dimer (aka O₄) observed at 20° elevation angle is correlated
442 with the lofted DOFS (Supplemental Figure S6). From this correlation we find that clear sky conditions
443 have 20° elevation angle O₄ dSCD > 10⁴³ molecule²cm⁻⁵ and use this cut to distinguish clear sky versus
444 clouds. To assure that GEOS-Chem results are only compared to the clear-sky observational data, we
445 apply this clear sky screen to the modeled BrO_{LTcol} timeseries. The use of this screen also assists in
446 minimizing variability in the averaging kernels and thus allowing the April averaged partial column
447 averaging kernels (Figure 3) to be applied for clear skies at any time of the year.



448

449 **Figure 4: Mean snowpack Br₂ emissions and p-Br⁻ by month, as simulated by GEOS-Chem.**

450 The top row shows emissions of Br₂ in the PHOTOPACK run, the middle row shows the emissions of
451 Br₂ in the PACK run, and the bottom row shows emissions of p-Br⁻ from adding the BLOW mechanism.



452 3. Examining reactive bromine in the Arctic spring

453 3.1 Snowpack Br₂ emissions

454 The top two rows of Figure 4 shows PHOTOPACK and PACK average snowpack Br₂ emissions
455 for each spring month. The emission of Br₂ in PHOTOPACK increases over the Arctic Ocean in May and
456 June, when the sun is above the horizon for up to 24 hours per day and ozone deposition yield is almost
457 always at the photo-enhanced level of 7.5%. Notably, Br₂ emissions over the Arctic Ocean in the
458 PHOTOPACK and BLOW+PHOTOPACK runs are highest in June when the sun is nearly always five
459 degrees above the horizon and surface temperatures may drop below freezing. The PACK emissions are
460 lower than the PHOTOPACK Br₂ emissions by an order of magnitude and shows a seasonal cycle with a
461 high BrO_{LTcol} in April and May with a decrease in May and June. While our ozone deposition velocities
462 (see Supplemental Figure S5) over Arctic sea ice are much higher than previous estimates of an
463 approximate magnitude of 0.01 cm/s (Toyota et al., 2011), the PHOTOPACK run highlights that a 75-
464 fold increase in daytime Br₂ yield can lead to predictions of increased Br₂ production over the North Pole
465 in June. Monthly satellite observations show that BrO reaches a minimum over the Arctic Ocean in June
466 (Richter et al., 1998).

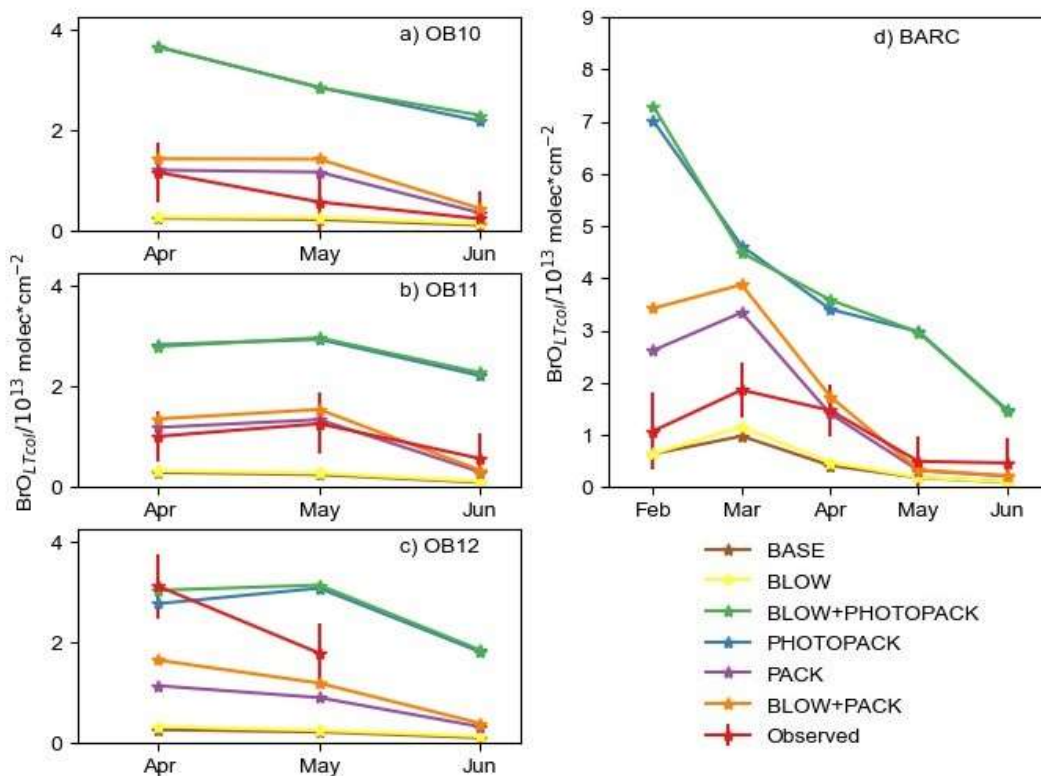
467 Coastal land regions within 200 km of the coastline have some of the highest modeled snowpack
468 Br₂ emissions (see Figure 4 rows 1 and 2). Dry deposition velocities are lower over ice covered ocean
469 than open ocean due to the higher likelihood of a stable surface boundary layer over the ice-covered
470 ocean (Toyota et al., 2016). This remains true within GEOS-Chem, as deposition rates are greatest over
471 land, less rapid over ice-covered ocean, and lowest over open ocean (see Supplemental Figure S5). Lower
472 dry deposition velocities over the ice-covered Arctic Ocean lead to decreased deposition and conversion
473 to Br₂. In GEOS-Chem, ozone mixing ratios and deposition are over three orders of magnitude larger than
474 BrNO₃ and HOBr mixing ratios and deposition over the Arctic Ocean, and ozone contributes more than
475 half of total Br₂ emitted in the PACK and BLOW+PACK runs. Our snowpack mechanism assumes that
476 all ozone deposited to the surface of a grid cell reacts with the snowpack cover and produces Br₂. This
477 assumption is more appropriate in the barren snow-covered coastal tundra but may be less accurate in
478 areas where deposition to vegetation dominates. This nonconservative approach may lead to
479 overestimation of Br₂ emissions from snowy vegetated surfaces. Our screens for snowpack emissions
480 described in section 1.3.5 tried to minimize these effects but may not work perfectly due to finite grid cell
481 resolution and other challenges. Increased Br₂ emissions observed in Figure 4 in northern Europe may
482 also be partially driven by increased local mixing ratios of ozone and NO_x over industrialized regions
483 such as the Kola Peninsula.



484 **3.2 Blowing Snow pBr⁻ emissions**

485 The bottom row of Figure 4 shows the total quantity of particulate bromide released by the
486 blowing snow SSA mechanism in the BLOW runs. Emissions over the Arctic Ocean decline each month
487 after the March maximum as rising temperatures increase the windspeed threshold for blowing snow SSA
488 production. Some icy coastal regions with frequently high windspeeds such as the Aleutian Islands south
489 of Alaska and the eastern coast of Greenland continue to emit SSA p-Br⁻ in April, and the extremely high
490 winds in the Aleutians enable SSA production into May. The location of specific high-wind storm
491 systems in spring 2015 may be evident in the darker red spots over the Arctic Ocean, which are
492 particularly noticeable over the Eurasian and Central Arctic in March. These monthly averages are only
493 accurate for the months in spring 2015 and may not be spatially representative of blowing snow SSA
494 production in other years.

495 The impact of the blowing snow SSA emissions is minimal on O-Buoys in the Beaufort Gyre,
496 possibly due to the spatial and seasonal variations in SSA p-Br⁻ emissions. Figure 4 shows that 2015 SSA
497 production was highest in March and April on the Eurasian and Central sector of the Arctic, and thus the
498 O-Buoys deployed as shown in Figure 2 are less exposed to the effects of SSA production than the Arctic
499 as a whole. Particulate bromide must be activated from SSA by heterogeneous reactions as in Figure 1,
500 leading to photochemical cycles that sustain further activation of bromide from SSA. The dearth of
501 sunlight over the Arctic Ocean in early March coincides with the greatest SSA p-Br⁻ production and
502 means that the increased February SSA p-Br⁻ emissions may not lead to a direct increase in BrO.



503

504 **Figure 5: Monthly average $\text{BrO}_{\text{LTcol}}$ in observations and model**

505 Monthly averages of BrO at a) O-Buoy 10, b) O-Buoy 11, c) O-Buoy 12, and d) BARC at Utqiagvik only
506 using predictions and observations when $\text{dSCDO}_4 > 1 \cdot 10^{43}$ molecules²cm⁻⁵. Observations with average 1σ
507 error shown in red. All units in 10¹³ molecules/cm².

508 3.3 Snowpack Br₂ emissions have more impact than blowing snow on monthly BrO abundance

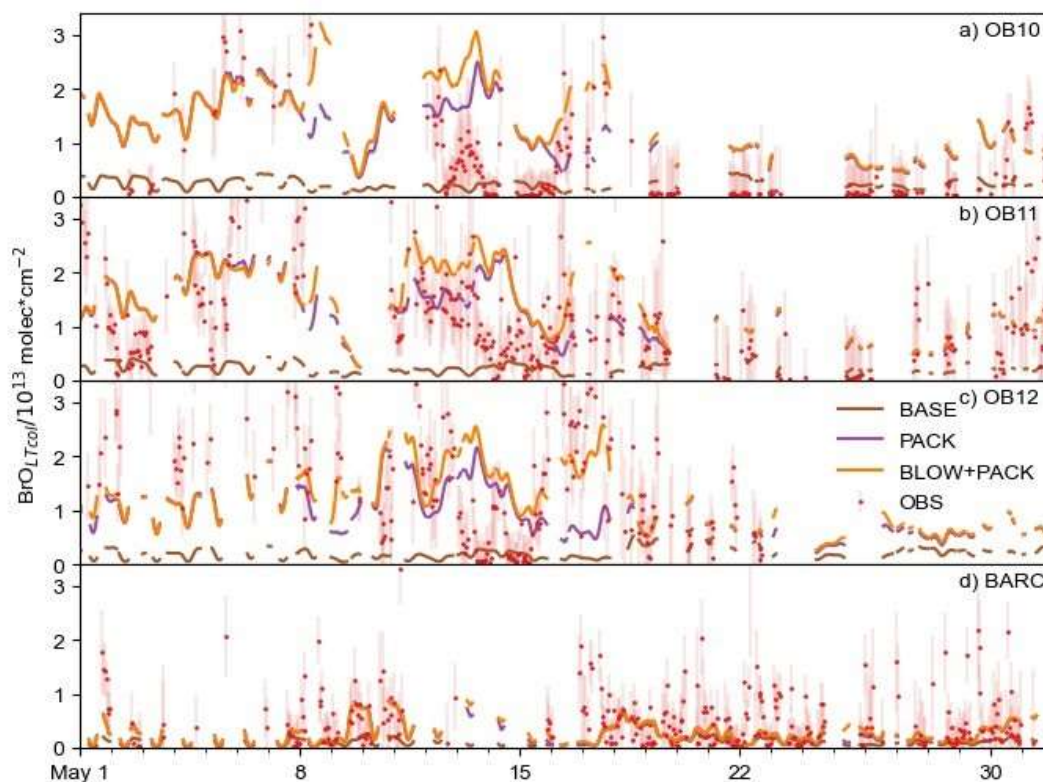
509 Increased levels of bromine have been historically seen at Utqiagvik during February, March,
510 April and May (Berg et al., 1983). Previous O-Buoy data analysis noted BrO dropping to zero in June
511 (Burd et al., 2017). Figure 5 shows monthly averaged modeled $\text{BrO}_{\text{LTcol}}$ at Utqiagvik and on the O-Buoys
512 for each model configuration. The difference in GEOS-Chem modeled monthly averaged $\text{BrO}_{\text{LTcol}}$ for O-
513 Buoys is minimal between the BASE and BLOW runs, the PHOTOPACK and BLOW+PHOTOPACK
514 runs, and the PACK and BLOW+PACK runs.

515 Both BASE and BLOW runs predict near-zero $\text{BrO}_{\text{LTcol}}$ on all O-Buoys and during most months
516 at Utqiagvik. The exception to this is the slight increases in monthly modeled $\text{BrO}_{\text{LTcol}}$ to $1 \cdot 10^{13}$
517 molecules/cm² in March and April. This BASE increase in $\text{BrO}_{\text{LTcol}}$ indicates that oceanic SSA rather than
518 blowing snow SSA can affect modeled BrO at Utqiagvik due to its closer proximity to open ocean regions



519 than the O-Buoys. The PACK and BLOW+PACK runs show the highest skill in reproducing
520 observations, falling within the monthly average of hourly measured $\text{BrO}_{\text{LTcol}}$ error for 9 of the 13 months
521 plotted in Figure 5. Both PACK and BLOW+PACK replicate the observed monthly pattern on O-Buoy 11
522 and at Utqiagvik especially well. The seasonal pattern of maximum modeled $\text{BrO}_{\text{LTcol}}$ at Utqiagvik in
523 March followed by a decrease to near-zero modeled $\text{BrO}_{\text{LTcol}}$ in May is replicated in both runs despite the
524 overprediction of $\text{BrO}_{\text{LTcol}}$ in February and March. The BLOW+PACK monthly $\text{BrO}_{\text{LTcol}}$ is between
525 $1 \cdot 10^{14}$ molecules/cm² and $1 \cdot 10^{13}$ molecules/cm² higher than PACK monthly $\text{BrO}_{\text{LTcol}}$ due to the addition
526 of blowing snow. This increase is most pronounced in February and March at Utqiagvik when lower
527 temperatures lead to lower threshold windspeeds and increased SSA production (see Supplemental Figure
528 S4).

529 The inclusion of increased daytime yield of snowpack Br_2 drives monthly average $\text{BrO}_{\text{LTcol}}$ above
530 $3 \cdot 10^{13}$ molecules/cm² in the PHOTOPACK and BLOW+PHOTOPACK runs from February until June,
531 far above peak observed monthly $\text{BrO}_{\text{LTcol}}$ of $2 \cdot 10^{13}$ molecules/cm². The PHOTOPACK and
532 BLOW+PHOTOPACK runs show steady decline in $\text{BrO}_{\text{LTcol}}$ from February to June at Utqiagvik.
533 Predictions of PHOTOPACK and BLOW+PHOTOPACK monthly June $\text{BrO}_{\text{LTcol}}$ above $2 \cdot 10^{13}$
534 molecules/cm² on the O-Buoys is due to increasing photo-assisted local snowpack Br_2 emissions over the
535 Arctic Ocean (see Figure 5). The PHOTOPACK mechanism predicts monthly average $\text{BrO}_{\text{LTcol}}$ within
536 observational error only on O-Buoy 12 in April. Aside from this replication of the sparsely sampled O-
537 Buoy 12 April $\text{BrO}_{\text{LTcol}}$, the PHOTOPACK mechanism overestimates $\text{BrO}_{\text{LTcol}}$. This overprediction of
538 $\text{BrO}_{\text{LTcol}}$ by PHOTOPACK and BLOW+PHOTOPACK extends to prediction of unrealistically high
539 mixing ratios for all tropospheric bromine species (see Supplemental Figure S7). This overprediction is a
540 product of high ozone deposition velocities and daytime conversion rates to Br_2 .



541
542 **Figure 6: Hourly BrO_{LTcol} timeseries**

543 Hourly timeseries of BLOW+PACK, PACK, and BASE BrO_{LTcol} on a) O-Buoy 10, b) O-Buoy 11, c) O-
544 Buoy 12 and d) BARC at Utqiagvik in the 2015 Arctic Spring. O-Buoy observations and error bars in red,
545 BASE BrO_{LTcol} in brown, PACK BrO_{LTcol} in purple, and BLOW+PACK BrO_{LTcol} in orange. All BrO_{LTcol}
546 plotted continuously except for gaps where dSCDO₄ > 1*10⁴³ molecules²cm⁻⁵.

547 **3.4 BLOW+PACK run best replicates hourly BrO events in mid and late May**

548 The model's hourly predictions of BrO_{LTcol} in May 2015 are shown in Figure 6 for the BASE,
549 PACK, and BLOW+PACK runs. The O-Buoys show fluctuations in observed BrO_{LTcol} during May and
550 show consistent increased columns of BrO_{LTcol} from May 10 to May 20. The BASE run never rises above
551 10¹³ molecules/cm² and underpredicts most May hourly BrO_{LTcol}, although BASE predicts monthly
552 BrO_{LTcol} on OB10 for two out of three months. Both PACK and BLOW+PACK runs show more skill in
553 replicating BrO_{LTcol}. The addition of the snowpack mechanism allows us to predict increased BrO_{LTcol} in
554 late May on O-Buoys 10 and 11. This points to the role of surface snowpack in late-season events in
555 agreement with the findings of Burd et al. (2017).

556 We can identify the role of blowing snow SSA by comparing the PACK and BLOW+PACK runs.
557 Both PACK and BLOW+PACK runs underestimate BrO_{LTcol} during the first ten days of May. BrO

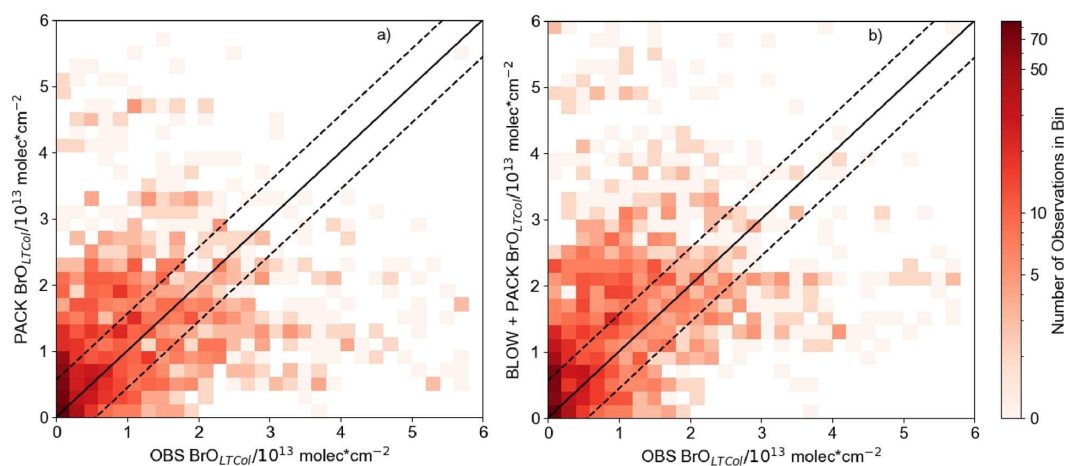


558 predictions and observations are more active starting on May 10. The blowing snow mechanism increases
559 BLOW+PACK $\text{BrO}_{\text{LTcol}}$ on May 12 and 13. PACK is skilled at replicating observed O-Buoy 11 $\text{BrO}_{\text{LTcol}}$
560 on both days, and both PACK and BLOW+PACK are within observational $\text{BrO}_{\text{LTcol}}$ error on May 13.

561 A BrO event also occurs on May 13 on O-Buoy 10. While the strength of the O-Buoy 10 BrO
562 event is overestimated by PACK and BLOW+PACK, the shape of that event is duplicated in both runs.
563 Examination of the O-Buoy 10 vertical Br_y profile in Supplemental Figure S7 shows surface BrO
564 increasing to 2 pmol/mol in the lowest 200 meters of the troposphere on May 10. BrO is mixed vertically
565 on May 12 and 13 throughout the lower troposphere, with a linear decrease from surface BrO mixing
566 ratios of 3 pmol/mol to 0 pmol/mol at 1200 m altitude. This May 12 $\text{BrO}_{\text{LTcol}}$ event is also associated with
567 surface ozone depletion to 15 nmol/mol.

568 Observed $\text{BrO}_{\text{LTcol}}$ decreases rapidly on all O-Buoys after May 14, and the model is unable to
569 track this sharp decrease. Rapid changes in $\text{BrO}_{\text{LTcol}}$ may be caused by sharp edges in BrO-enriched
570 air masses such as those seen by Simpson et al. (2017). GEOS-Chem run at this resolution cannot replicate
571 abrupt changes in BrO, but it does slowly decrease $\text{BrO}_{\text{LTcol}}$ to reach $\text{BrO}_{\text{LTcol}}$ to less than 10^{13}
572 molecules/cm² on May 16. The BLOW+PACK mechanism is skilled in replicating the magnitude and
573 features of a mid-May BrO event on several O-Buoys.

574 Figure 7 shows all Spring 2015 $\text{BrO}_{\text{LTcol}}$ observations on O-Buoys 10, 11, 12, and BARC plotted
575 against PACK $\text{BrO}_{\text{LTcol}}$ and BLOW+PACK $\text{BrO}_{\text{LTcol}}$. The increase in $\text{BrO}_{\text{LTcol}}$ on adding BLOW leads to
576 fewer underpredictions of observations (see bottom right section of Figure 7b). The Pearson correlation
577 coefficient (r) between PACK $\text{GCBro}_{\text{LTcol}}$ and observed $\text{BrO}_{\text{LTcol}}$ is 0.33, improving to 0.39 on addition of
578 BLOW in the BLOW+PACK run. Other runs show less skill in replicating observations, with a BASE
579 $\text{BrO}_{\text{LTcol}}$ Pearson correlation to observations of 0.19 and a BLOW $\text{BrO}_{\text{LTcol}}$ Pearson correlation to
580 observations of 0.23. We also performed a simple linear regression to determine the relationship between
581 predictions and observations for each run. The slope of the line of best fit improves drastically on addition
582 of PACK, changing from 0.06 for BASE and 0.07 for BLOW to 0.33 for PACK and 0.44 for
583 BLOW+PACK. There is a positive synergistic effect on the slope of the line of best fit when using both
584 BLOW and PACK in combination rather than individually. The use of both BLOW and PACK
585 mechanisms implements literature findings on the processes influencing Arctic reactive bromine and
586 increases correlation between GEOS-Chem predictions and observations.



587

588 **Figure 7: Hourly modeled $\text{BrO}_{\text{LTcol}}$ versus $\text{BrO}_{\text{LTcol}}$ observations**

589 Two dimensional histograms showing density of GEOS-Chem predicted BrO versus all Spring 2015
590 hourly $\text{BrO}_{\text{LTcol}}$, with a) PACK $\text{BrO}_{\text{LTcol}}$ shown at left sorted into square bins of 0.2 with an Pearson r
591 correlation to observations of 0.33 and b) BLOW+PACK $\text{BrO}_{\text{LTcol}}$ on the bottom sorted into square bins
592 of 0.2 with Pearson r correlation to observations to 0.39. All units are in molecules/ cm^2 . 1:1 line drawn in
593 the center in black, with a margin of the average observational error plotted in dashed black lines around
594 the central 1:1 line.

595 4. Arctic Spring reactive bromine modeling discussion

596 4.1 Use of both mechanisms in conjunction leads to best prediction of tropospheric BrO results

597 Initial implementation of this snowpack mechanism in Toyota et al. (2011) increased the daytime
598 yield of Br_2 from ozone depletion to 7.5% to improve agreement between observed and modeled surface
599 ozone mixing ratios. Toyota et al. (2011) also increased the surface resistance of ozone to 10000 s/m,
600 decreased deposition velocities on Arctic snowpack to approximately 0.01 cm/s. Our model using a
601 constant yield of Br from ozone deposition performs best, despite observations that sunlight has an effect
602 on reactive bromine recycling in the snowpack (Pratt et al., 2013; Custard et al., 2017). GEOS-Chem does
603 not explicitly model heterogeneous photochemistry within the snowpack interstitial space but does
604 include heterogeneous bromine chemistry on aerosol particle surfaces after the Br_2 is emitted from the
605 snowpack into the lowest model layer. The updates to GEOS-Chem halogen chemistry (Schmidt et al.,
606 2016; Sherwen et al., 2016b; Chen et al., 2017; Wang et al., 2019b) should be mechanistically sufficient
607 to model daytime heterogeneous chemistry of reactive bromine on aerosol surfaces. We note that
608 improvements to GEOS-Chem have increased the explicit modeling of these photochemical recycling and
609 amplification processes, possibly reducing the need for empirical increases to daytime yields.

610 Our findings differ from recent implementations of the snowpack mechanism in Herrmann et al.
611 (2021) and Marelle et al. (2021). While all snowpack mechanisms are based on Toyota et al. (2011),



612 several large differences in model configuration and mechanism implementation explain these
613 differences. We allow Br₂ production from ozone deposition over all snow surfaces, leading to much
614 higher Br₂ production over MYI and coastal regions. Land snowpack can produce Br₂ on exposure to
615 ozone and sunlight (Pratt et al., 2013; Custard et al., 2017) and Figure 4 shows our coastal snowpack
616 producing large quantities of Br₂. Tropospheric reactive bromine chemistry has been observed up to 200
617 km inland from the coast (Peterson et al., 2018). Marelle et al. (2021) underestimates BrO in late March
618 and overestimates Utqiagvik BrO in early April. This seasonal pattern may be due to increased daytime
619 ozone yield on first year ice near Utqiagvik in April. Herrmann et al. (2021) found that HOBr and BrNO₃
620 deposition was more important in driving snowpack Br₂ production and that the daytime yield of 7.5%
621 Br₂ on ozone deposition underpredicted BrO. We find that ozone contributes slightly more than HOBr
622 and BrNO₃ because we allow for Br₂ production on ozone deposition over multi-year ice and coastal
623 snowpack regions. The temporal scale of this manuscript spans the entire year, while Herrmann et al.
624 (2021) only spans February, March, and April. Our longer timescale highlights the issue of increased
625 daytime Br₂ yield during May and June (see Figure 4 PHOTOPACK) with increased emissions over the
626 Arctic Ocean that are not in agreement with satellite observations of minimal Arctic tropospheric BrO in
627 June (Richter et al., 1998).

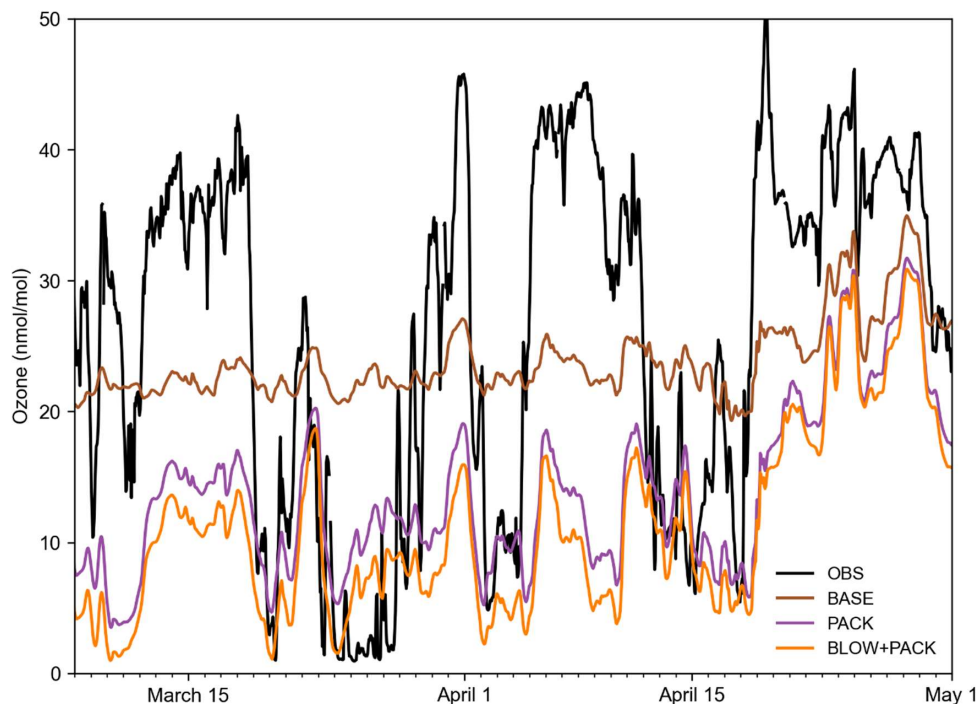
628 **4.2 Addition of PACK mechanism increases surface ozone predictive skill**

629 The Barrow Arctic Research Center (BARC) in Utqiagvik has the most comprehensive coverage
630 of surface ozone in Spring 2015. A constant yield of 0.1% Br₂ from ozone deposition allows us to
631 approximate the average vertical extent of ozone depletion events at Utqiagvik in May 2015. The increase
632 in Br_y in the PACK and BLOW+PACK runs is confined to the lowest 1000 m of the atmosphere (see
633 Supplemental Figure S7). Ozone depletions, caused by reactive bromine chemistry, often only occur
634 within the lowest 1000 m of the troposphere (Bottenheim et al., 2002; Salawitch et al., 2010). Previous
635 studies have found evidence of lofted BrO in plumes at altitudes up to 900 m AGL (Peterson et al., 2017).
636 The monthly average Utqiagvik May surface ozone in BLOW and BLOW+PACK is 22 nmol/mol,
637 matching mean May surface ozone from 1999-2008 (Oltmans et al., 2012). The PHOTOPACK runs
638 generate mean May surface ozone depletion to approximately 5 nmol/mol, far below the May mean. The
639 PACK and BLOW+PACK runs duplicate the approximate vertical extent of elevated bromine levels and
640 the strength of historic May ozone depletion.

641 Figure 8 shows hourly ozone predictions alongside BARC ozone observations (McClure-Begley,
642 Petropavlovskikh, and Oltmans, 2014). The BASE model fails to replicate variance in ozone measured at
643 BARC in Utqiagvik, with a Pearson correlation coefficient to observations of 0.35. Adding PACK
644 improves Pearson correlation to 0.47, within rounding error of BLOW+PACK Pearson correlation of



645 0.47. Both PACK and BLOW+PACK significantly improve model performance in replicating ozone
646 depletions in such as the depletion below 30 nmol/mol from March 20 to March 29 but fail to track the
647 subsequent recovery of ozone to background levels on April 1. Predicted PACK ozone does not recover
648 to backgrounds levels until a height of roughly 1000 m. A similar pattern where our model replicates low
649 ozone but fails to predict the recovery of ozone to background levels occurs on April 5 and 15. Previous
650 modeling of Utqiaġvik spring 2012 ozone in WRF-Chem found a similar linear correlation coefficient of
651 0.5 to BROMEX observations (Simpson et al., 2017) when using both blowing snow and snowpack
652 mechanisms (Marelle et al., 2021). We are biased low compared to observations, with a root mean square
653 error of 17.0 nmol/mol compared to a root mean square error of 12.9 nmol/mol in Marelle et al. (2021).
654 This may be partially due to limited vertical resolution in GEOS-Chem that may be inadequate to describe
655 shallow surface-based temperature inversions and subsequent recovery. The high bias in ozone deposition
656 velocity over sea ice surfaces may also contribute to low ozone mixing ratios near the surface.



657

658 **Figure 8: Hourly Utqiaġvik ozone timeseries**

659 Hourly timeseries of BLOW+PACK, PACK, and BASE ozone Utqiaġvik in the 2015 Arctic Spring.
660 Ozone observations at BARC in black (McClure-Begley, Petropavlovskikh and Oltmans, 2014), BASE
661 ozone in brown, PACK ozone in purple, and BLOW+PACK ozone in orange. Gaps indicate missing
662 observational data.

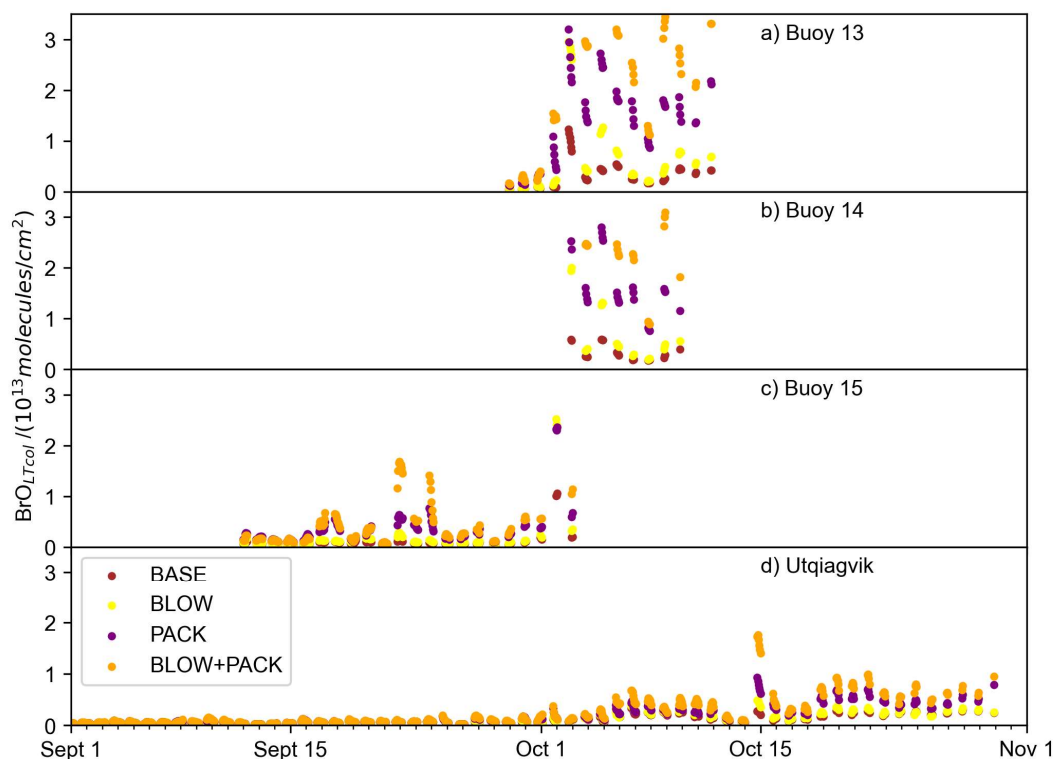


663 5. Examining reactive bromine in the Arctic in September and October

664 O-Buoys deployed during fall 2015 measured BrO slant column densities characterized by noise
665 around zero (see Supplemental Figures S8 and S9). We do not retrieve vertical column density from these
666 fall slant column densities, because the resulting retrievals would be biased positive due to an algorithm
667 requirement that only positive BrO column densities are allowed in the optimal estimation inversion.
668 These differential slant column densities (dSCDs) can be used qualitatively to determine the presence or
669 absence of BrO above the detection limit. If the dSCDs display noise around zero at all viewing angles,
670 the BrO in the troposphere is below the detection limit of the spectrometer. The pattern of larger BrO
671 dSCDs at near-horizon viewing elevation angles observed at Utqiagvik during Arctic Spring in 2015
672 Supplemental Figure S7, indicate the presence of tropospheric BrO above the detection limit, which only
673 occur during Arctic spring. Any BrO present in the Arctic troposphere in September and October falls
674 below detection limits at Utqiagvik (see Supplemental Figure S8) and on each O-Buoy (see Supplemental
675 Figure S9). The average Arctic Spring 2015 MAX-DOAS $\text{BrO}_{\text{LTcol}}$ detection limits are 5×10^{12}
676 molecules/cm² (Peterson et al., 2015; Simpson et al., 2017; Swanson et al., 2020). Both BLOW and
677 PACK mechanisms lead to prediction of increased fall BrO because the weather and sea ice conditions
678 specified in the emission algorithms occur in fall as well as spring.

679 Figure 9 shows fall predictions of $\text{BrO}_{\text{LTcol}}$ filtered for times when solar elevation angle was
680 greater than 5°. BASE and SNOW $\text{BrO}_{\text{LTcol}}$ remain near zero in September but rise above the MAX-
681 DOAS detection limit of 5×10^{12} molecules/cm² $\text{BrO}_{\text{LTcol}}$ in October. The addition of the blowing snow
682 mechanism propels BLOW $\text{BrO}_{\text{LTcol}}$ up to 6×10^{13} molecules/cm² in October. O-Buoys 13 and 14 have
683 the highest modeled fall $\text{BrO}_{\text{LTcol}}$ but even Utqiagvik has several days of $\text{BrO}_{\text{LTcol}}$ above 5×10^{12}
684 molecules/cm² in late October. There is no clear evidence of any BrO above MAX-DOAS detection limits
685 at Utqiagvik or on any O-Buoy in October, as seen by the dSCDs scattered around zero in Supplemental
686 Figures S8 and S9.

687



688

689 **Figure 9: Fall GEOS-Chem Predicted $\text{BrO}_{\text{LTcol}}$**

690 Hourly timeseries of BLOW+PACK, PACK, and BASE $\text{BrO}_{\text{LTcol}}$ on a) O-Buoy 10, b) O-Buoy 11, c) O-
691 Buoy 12 and d) BARC at Utqiagvik during September and October 2015 BASE $\text{BrO}_{\text{LTcol}}$ in brown, PACK
692 $\text{BrO}_{\text{LTcol}}$ in purple, and BLOW+PACK $\text{BrO}_{\text{LTcol}}$ in orange. All $\text{BrO}_{\text{LTcol}}$ plotted continuously except for
693 gaps where solar elevation angle was less than 5° .

694 Both mechanisms assume that snowpack and SSA are just as capable of recycling reactive
695 bromine as in the springtime. High fall and winter SSA agrees with observations of peak SSA during
696 polar winter in both Antarctica (Wagenbach et al., 1998) and in the Arctic (Jacobi et al., 2012). The
697 deposition of Arctic haze (Douglas and Sturm, 2004) and SSA (Jacobi et al., 2019) increases snowpack
698 salinity and sulfate content over the course of winter and spring. This seasonal change in snowpack
699 salinity and acidity may enable reactive bromine recycling in the Arctic Spring, but there may not
700 sufficient haze and SSA deposition in fall to decrease snowpack pH and increase snowpack bromide
701 content. Additional observations of fall snowpack over sea ice including ion content could show different
702 snowpack composition in spring and fall. Thus the GEOS-Chem model overestimates fall BrO by
703 assuming the fall snowpack is equally capable of reactive bromine recycling as spring snowpack, possibly
704 due to the assumption of an infinite reservoir of snowpack bromide in all seasons. Most other modeling



705 exercises have focused on spring with unknown predictions in fall, possibly indicating problems in
706 mechanisms or parameterizations being employed, so we suggest that modeling should be done for a full
707 year to improve underlying chemistry and physics.

708 6. Conclusions

709 We add snowpack Br₂ production to GEOS-Chem based on multiple field observations
710 demonstrating molecular bromine production in snowpack interstitial air. We use a mechanistic
711 parameterization of snowpack Br₂ production based on Toyota et al. (2011) in which Br₂ is emitted from
712 all snowpack of sufficient salinity and depth over land and sea ice upon deposition of the precursor
713 species HOBr, BrNO₃, and ozone. Prior work has also added a blowing snow SSA production mechanism
714 that increases aerosol particulate bromide and thus facilitates heterogeneous recycling of reactive bromine
715 on these aerosol particle surfaces. We update the halogen scheme to GEOS-Chem 12.9.3 and performed
716 six model simulations including a BASE run with neither blowing snow nor snowpack emissions, a
717 PACK run assuming constant yield of Br₂ on ozone deposition over all snow surfaces, a PHOTOPACK
718 run assuming increased daytime yield of Br₂ on ozone deposition (similar in Toyota et al., 2011), a
719 BLOW run using only blowing snow SSA formation and two additional runs combining BLOW and each
720 respective PACK mechanism. The increased daytime yield of Br₂ in PHOTOPACK leads to
721 overprediction of BrO in these simulations, but the PACK run (with constant Br₂ yield day and night)
722 matches monthly averaged BrO vertical column densities for 9 of 13 cases at O-Buoy and Utqiagvik in
723 springtime months. The PACK and BLOW+PACK runs were successful in replicating observed mid-May
724 BrO events on O-Buoys as well as recurrence events at the end of May. The BLOW mechanism
725 effectively increases aerosol surface available for turnover of reactive bromine. The snowpack
726 mechanism has more impact on modeled BrO mixing ratios than the blowing snow mechanism, but both
727 contribute to tropospheric reactive bromine. We extend our model run to the full year and find that
728 enhanced daytime Br₂ yield can lead to increased Arctic Ocean Br₂ production in the summer. Examining
729 modeled BrO in fall 2015 reveals prediction of BrO when using these mechanisms that are at odds with
730 observations.

731 The inclusion of two Arctic reactive bromine production mechanisms based on literature
732 observations of snowpack Br₂ emission and blowing snow SSA formation improves model skill in
733 replicating Arctic tropospheric BrO in spring 2015. The snowpack is an important source of reactive
734 bromine, and SSA particles provide an abundant surface for sustained reactive bromine recycling in the
735 troposphere. We find that using both snowpack and blowing snow bromine production mechanisms is
736 necessary for modeling BrO in the Arctic.

737 *Competing interests:* The authors declare that they have no conflict of interest.



738 Author contributions. WFS, WRS and CH designed the study. WRS collected and curated MAX-DOAS
739 data. KC, LM, JT, LJ, JH and contributed code for reactive bromine mechanisms. CH, KC, LJ, JH, BA,
740 SZ, QC, XW, and TS contributed model updates. WFS carried out modeling and analysis. WFS wrote the
741 paper with input from all authors.

742 **7. Acknowledgements**

743 We acknowledge support from the National Science Foundation for providing funding under grants ARC-
744 1602716, AGS-1702266, AGS-2109323, and ARC-1602883. This work also supported by the CNRS
745 INSU LEFE-CHAT program under the grant Brom-Arc, and NASA grant 80NSSC19K1273. This
746 research has received funding from the European Union's Horizon 2020 research and innovation program
747 under grant agreement no. 689443 via project iCUPE (Integrative and Comprehensive Understanding on
748 Polar Environments). The O-Buoy and Utqiagvik ground-based BrO datasets are available in the
749 arcticdata.io repository (doi:10.18739/A2WD4W). We recognize the work of Jiayue Huang in adding the
750 blowing snow SSA mechanism to GEOS-Chem. We would like to thank the National Oceanic and
751 Atmospheric Administration (NOAA) Global Monitoring Division for the provision of ozone and
752 temperature data near Utqiagvik available online at doi:10.7289/V57P8WBF. We acknowledge use of the
753 coastline distance dataset from the Pacific Islands Ocean Observing System. We acknowledge the use of
754 imagery from the Land Atmosphere Near Real-Time Capability for EOS (LANCE) system and services
755 from the Global Imagery Browse Services (GIBS), both operated by the NASA/GSFC/Earth Science Data
756 and Information System (ESDIS, <https://earthdata.nasa.gov>) with funding provided by NASA/HQ. We
757 owe a debt of gratitude to all members of the Atmospheric Chemistry and Global Change group at Florida
758 State University for their support for working with GEOS-Chem and Python. We thank the global GEOS-
759 Chem community for their tireless work to improve the model. We also thank all involved in the O-Buoy
760 project for data collection and analysis.

761 **8. References**

- 762 AMAP: Arctic Monitoring and Assessment Program 2011: Mercury in the Arctic., 2011.
- 763 Artiglia, L., Edebeli, J., Orlando, F., Chen, S., Lee, M. T., Corral Arroyo, P., Gilgen, A., Bartels-Rausch,
764 T., Kleibert, A., Vazdar, M., Andres Carignano, M., Francisco, J. S., Shepson, P. B., Gladich, I. and
765 Ammann, M.: A surface-stabilized ozonide triggers bromide oxidation at the aqueous solution-vapour
766 interface, *Nat. Commun.*, 8(1), 1–7, doi:10.1038/s41467-017-00823-x, 2017.
- 767 Bariteau, L., Helmig, D., Fairall, C. W., Hare, J. E., Hueber, J. and Lang, E. K.: Determination of oceanic
768 ozone deposition by ship-borne eddy covariance flux measurements, *Atmos. Meas. Tech.*, 3(2), 441–455,
769 doi:10.5194/amt-3-441-2010, 2010.
- 770 Barrie, L. A., Bottenheim, J. W., Schnell, R. C., Crutzen, P. J. and Rasmussen, R. A.: Ozone destruction
771 and photochemical reactions at polar sunrise in the lower Arctic atmosphere, *Nature*, 334(6178), 138–
772 141, doi:10.1038/334138a0, 1988.



- 773 Berg, W. W., Sperry, P. D., Rahn, K. A. and Gladney, E. S.: Atmospheric Bromine in the Arctic, *J.*
774 *Geophys. Res.*, 88(3), 6719–6736, doi:10.1029/JC088iC11p06719, 1983.
- 775 Bey, I., Jacob, D. J., Yantosca, R. M., Logan, J. A., Field, B. D., Fiore, A. M., Li, Q., Liu, H. Y., Mickley,
776 L. J. and Schultz, M. G.: Global modeling of tropospheric chemistry with assimilated meteorology:
777 Model description and evaluation, *J. Geophys. Res. Atmos.*, 106(D19), 23073–23095,
778 doi:10.1029/2001JD000807, 2001.
- 779 Bottenheim, J. W., Fuentes, J. D., Tarasick, D. W. and Anlauf, K. G.: Ozone in the Arctic lower
780 troposphere during winter and spring 2000 (ALERT2000), *Atmos. Environ.*, 36, 2535–2544, 2002.
- 781 Burd, J. A., Peterson, P. K., Nghiem, S. V., Perovich, D. K. and Simpson, W. R.: Snow Melt Onset
782 Hinders Bromine Monoxide Heterogeneous Recycling in the Arctic, *J. Geophys. Res. Atmos.*, 1–13,
783 doi:10.1002/2017JD026906, 2017.
- 784 Cao, L., Platt, U. and Gutheil, E.: Role of the boundary layer in the occurrence and termination of the
785 tropospheric ozone depletion events in polar spring, *Atmos. Environ.*, 132, 98–110,
786 doi:10.1016/j.atmosenv.2016.02.034, 2016.
- 787 Carlson, D., Donohoue, D., Platt, U. and Simpson, W. R.: A low power automated MAX-DOAS
788 instrument for the Arctic and other remote unmanned locations, *Atmos. Meas. Tech.*, 429–439, 2010.
- 789 Chance, K.: Analysis of BrO Measurements from the Global Ozone Monitoring Experiment, *Geophys.*
790 *Res. Lett.*, 25(17), 3335–3338, 1998.
- 791 Chen, Q., Schmidt, J. A., Shah, V., Jaeglé, L., Sherwen, T. and Alexander, B.: Sulfate production by
792 reactive bromine: Implications for the global sulfur and reactive bromine budgets, *Geophys. Res. Lett.*,
793 44(13), 7069–7078, doi:10.1002/2017GL073812, 2017.
- 794 Choi, S., Wang, Y., Salawitch, R. J., Canty, T., Joiner, J., Zeng, T., Kurosu, T. P., Chance, K., Richter,
795 A., Huey, L. G., Liao, J., Neuman, J. A., Nowak, J. B., Dibb, J. E., Weinheimer, A. J., Diskin, G.,
796 Ryerson, T. B., Da Silva, A., Curry, J., Kinnison, D., Tilmes, S. and Levelt, P. F.: Analysis of satellite-
797 derived Arctic tropospheric BrO columns in conjunction with aircraft measurements during ARCTAS and
798 ARCPAC, *Atmos. Chem. Phys.*, 12(3), 1255–1285, doi:10.5194/acp-12-1255-2012, 2012.
- 799 von Clarmann, T. and Glatthor, N.: The application of mean averaging kernels to mean trace gas
800 distributions, *Atmos. Meas. Tech. Discuss.*, 1–11, doi:10.5194/amt-2019-61, 2019.
- 801 Clemer, K., Van Roozendaal, M., Fayt, C., Hendrick, F., Hermans, C., Pinardi, G., Spurr, R., Wang, P.
802 and Maziere, M. De: Multiple wavelength retrieval of tropospheric aerosol optical properties from
803 MAXDOAS measurements in Beijing, *Atmos. Meas. Tech.*, 3, 863–878, doi:10.5194/amt-3-863-2010,
804 2010.
- 805 Custard, K. D., Raso, A. R. W., Shepson, P. B., Staebler, R. M. and Pratt, K. A.: Production and Release
806 of Molecular Bromine and Chlorine from the Arctic Coastal Snowpack, *ACS Earth Sp. Chem.*, 1, 142–
807 151, doi:10.1021/acsearthspacechem.7b00014, 2017.
- 808 Dery, S. J. and Yau, M. K.: A Bulk Blowing Snow Model, *Bound. Layer Meteorol.*, 93, 237–251, 1999.
- 809 Déry, S. J. and Yau, M. K.: Simulation of blowing snow in the Canadian Arctic using a double-moment
810 model, *Boundary-Layer Meteorol.*, 99(2), 297–316, doi:10.1023/A:1018965008049, 2001.
- 811 Domine, F., Sparapani, R., Ianniello, A. and Beine, H. J.: The origin of sea salt in snow on Arctic sea ice
812 and in coastal regions, *Atmos. Chem. Phys. Discuss.*, 4(4), 4737–4776, doi:10.5194/acpd-4-4737-2004,
813 2004.



- 814 Douglas, T. A. and Sturm, M.: Arctic haze, mercury and the chemical composition of snow across
815 northwestern Alaska, *Atmos. Environ.*, doi:10.1016/j.atmosenv.2003.10.042, 2004.
- 816 Eastham, S. D., Weisenstein, D. K. and Barrett, S. R. H.: Development and evaluation of the unified
817 tropospheric-stratospheric chemistry extension (UCX) for the global chemistry-transport model GEOS-
818 Chem, *Atmos. Environ.*, 89, 52–63, doi:10.1016/j.atmosenv.2014.02.001, 2014.
- 819 Falk, S. and Sinnhuber, B. M.: Polar boundary layer bromine explosion and ozone depletion events in the
820 chemistry-climate model EMAC v2.52: Implementation and evaluation of AirSnow algorithm, *Geosci.
821 Model Dev.*, 11(3), 1115–1131, doi:10.5194/gmd-11-1115-2018, 2018.
- 822 Fan, S. M. and Jacob, D. J.: Surface ozone depletion in Arctic spring sustained by bromine reactions on
823 aerosols, *Nature*, 359(6395), 522–524, doi:10.1038/359522a0, 1992.
- 824 Fischer, E. V., Jacob, D. J., Yantosca, R. M., Sulprizio, M. P., Millet, D. B., Mao, J., Paulot, F., Singh, H.
825 B., Roiger, A., Ries, L., Talbot, R. W., Dzepina, K. and Pandey Deolal, S.: Atmospheric peroxyacetyl
826 nitrate (PAN): A global budget and source attribution, *Atmos. Chem. Phys.*, 14(5), 2679–2698,
827 doi:10.5194/acp-14-2679-2014, 2014.
- 828 Fisher, J. A., Jacob, D. J., Travis, K. R., Kim, P. S., Marais, E. A., Miller, C. C., Yu, K., Zhu, L.,
829 Yantosca, R. M., Sulprizio, M. P., Mao, J., Wennberg, P. O., Crounse, J. D., Teng, A. P., Nguyen, T. B.,
830 Clair, J. M. S., Cohen, R. C., Romer, P., Nault, B. A., Wooldridge, P. J., Jimenez, J. L., Campuzano-Jost,
831 P., Day, D. A., Hu, W., Shepson, P. B., Xiong, F., Blake, D. R., Goldstein, A. H., Misztal, P. K., Hanisco,
832 T. F., Wolfe, G. M., Ryerson, T. B., Wisthaler, A. and Mikoviny, T.: Organic nitrate chemistry and its
833 implications for nitrogen budgets in an isoprene- and monoterpene-rich atmosphere: Constraints from
834 aircraft (SEAC4RS) and ground-based (SOAS) observations in the Southeast US, *Atmos. Chem. Phys.*,
835 16(9), 5969–5991, doi:10.5194/acp-16-5969-2016, 2016.
- 836 Foster, K. L., Plastring, R. A., Bottenheim, J. W., Shepson, P. B., Finlayson-pitts, B. J. and Spicer, C.
837 W.: The Role of Br₂ and BrCl in Surface Ozone Destruction at Polar Sunrise, *Science* (80-.),
838 291(JANUARY), 471–475, 2001.
- 839 Frey, M. M., Norris, S. J., Brooks, I. M., Anderson, P. S., Nishimura, K., Yang, X., Jones, A. E.,
840 Nerentorp Mastromonaco, M. G., Jones, D. H. and Wolff, E. W.: First direct observation of sea salt
841 aerosol production from blowing snow above sea ice, *Atmos. Chem. Phys.*, (April), 1–53,
842 doi:10.5194/acp-2019-259, 2020.
- 843 Frieß, U., Monks, P. S., Remedios, J. J., Rozanov, A., Sinreich, R., Wagner, T. and Platt, U.: MAX-
844 DOAS O₄ measurements: A new technique to derive information on atmospheric aerosols: 2. Modeling
845 studies, *J. Geophys. Res.*, 111, 20, doi:10.1029/2005JD006618, 2006.
- 846 Frieß, U., Beirle, S., Bonilla, L. A., Bösch, T., Friedrich, M. M., Hendrick, F., Piders, A., Richter, A.,
847 Roozendaal, M. Van, Rozanov, V. V., Spinei, E. and Tzipitz, J.: Intercomparison of MAX-DOAS vertical
848 profile retrieval algorithms : studies using synthetic data, *Atmos. Meas. Tech.*, (2), 2155–2181, 2019.
- 849 Gelaro, R., McCarty, W., Suarez, M. J., Todling, R., Molod, A., Takacs, L., Randles, C., Darmenov, A.,
850 Bosilovich, M., Reichle, R., Wargan, K., Coy, L., Cullather, R., Draper, C., Akella, S., Buchard, V.,
851 Conaty, A., Da Silva, A., Gu, W., Kim, G., Koster, R., Lucchesi, R., Merkova, D., Nielsen, J. E., Partyka,
852 G., Pawson, S., Putman, W., Rienecker, M., Schubert, S., Sienkiewicz, M. and Zhao, B.: The Modern-Era
853 Retrospective Analysis for Research and Applications , *J. Clim.*, 30, 5419–5454, doi:10.1175/JCLI-D-16-
854 0758.1, 2017.
- 855 Group, N. O. B. P. and Stumpf, R.: Distance to Nearest Coastline: 0.01 Degree Grid, [online] Available
856 from: https://pae-paha.pacioos.hawaii.edu/thredds/ncss/dist2coast_1deg/dataset.html, 2021.



- 857 Halfacre, J. W., Knepp, T. N., Shepson, P. B., Thompson, C. R., Pratt, K. A., Li, B., Peterson, P. K.,
858 Walsh, S. J., Simpson, W. R., Matrai, P. A., Bottenheim, J. W., Netcheva, S., Perovich, D. K. and Richter,
859 A.: Temporal and spatial characteristics of ozone depletion events from measurements in the Arctic,
860 *Atmos. Chem. Phys.*, 14(10), 4875–4894, doi:10.5194/acp-14-4875-2014, 2014.
- 861 Halfacre, J. W., Shepson, P. B. and Pratt, K. A.: pH-dependent production of molecular chlorine,
862 bromine, and iodine from frozen saline surfaces, *Atmos. Chem. Phys.*, 19, 4917–4931, 2019.
- 863 Herrmann, M., Sihler, H., Frieß, U., Wagner, T., Platt, U. and Gutheil, E.: Time-dependent 3D
864 simulations of tropospheric ozone depletion events in the Arctic spring using the Weather Research and
865 Forecasting model coupled with Chemistry (WRF-Chem), , 7611–7638, 2021.
- 866 Holmes, C. D., Jacob, D. J., Corbitt, E. S., Mao, J., Yang, X., Talbot, R. and Slemr, F.: Global
867 atmospheric model for mercury including oxidation by bromine atoms, *Atmos. Chem. Phys.*, 10(24),
868 12037–12057, doi:10.5194/acp-10-12037-2010, 2010.
- 869 Hönniger, G. and Platt, U.: Observations of BrO and its vertical distribution during surface ozone
870 depletion at Alert, *Atmos. Environ.*, 36(15–16), 2481–2489, doi:10.1016/S1352-2310(02)00104-8, 2002.
- 871 Hönniger, G., von Friedeburg, C. and Platt, U.: Multi Axis Differential Optical Absorption Spectroscopy
872 (MAX-DOAS), *Atmos. Chem. Phys.*, 4, 231–254, doi:10.5194/acpd-3-5595-2003, 2004.
- 873 Huang, J. and Jaeglé, L.: Wintertime enhancements of sea salt aerosol in polar regions consistent with a
874 sea-ice source from blowing snow, *Atmos. Chem. Phys.*, (November), 1–23, doi:10.5194/acp-2016-972,
875 2017.
- 876 Huang, J., Jaeglé, L. and Shah, V.: Using CALIOP to constrain blowing snow emissions of sea salt
877 aerosols over Arctic and Antarctic sea ice, *Atmos. Chem. Phys.*, 16253–16269, 2018.
- 878 Huang, J., Jaeglé, L., Chen, Q., Alexander, B., Sherwen, T., Evans, M., Theys, N. and Choi, S.:
879 Evaluating the impact of blowing snow sea salt aerosol on springtime BrO and O₃ in the Arctic, *Atmos.*
880 *Chem. Phys.*, 1–36, doi:10.5194/acp-2019-1094, 2020.
- 881 Jacobi, H. W., Voisin, D., Jaffrezo, J. L., Cozic, J. and Douglas, T. A.: Chemical composition of the
882 snowpack during the OASIS spring campaign 2009 at Barrow, Alaska, *J. Geophys. Res. Atmos.*,
883 doi:10.1029/2011JD016654, 2012.
- 884 Jacobi, H. W., Obleitner, F., Da Costa, S., Ginot, P., Eleftheriadis, K., Aas, W. and Zannata, M.:
885 Deposition of ionic species and black carbon to the Arctic snowpack: Combining snow pit observations
886 with modeling, *Atmos. Chem. Phys.*, 19(15), 10361–10377, doi:10.5194/acp-19-10361-2019, 2019.
- 887 Jaeglé, L., Quinn, P. K., Bates, T. S., Alexander, B. and Lin, J. T.: Global distribution of sea salt aerosols:
888 New constraints from in situ and remote sensing observations, *Atmos. Chem. Phys.*, 11(7), 3137–3157,
889 doi:10.5194/acp-11-3137-2011, 2011.
- 890 Keller, C. A., Long, M. S., Yantosca, R. M., Da Silva, A. M., Pawson, S. and Jacob, D. J.: HEMCO v1.0:
891 A versatile, ESMF-compliant component for calculating emissions in atmospheric models, *Geosci. Model*
892 *Dev.*, 7(4), 1409–1417, doi:10.5194/gmd-7-1409-2014, 2014.
- 893 Knepp, T. N., Bottenheim, J., Carlsen, M., Carlson, D., Donohoue, D., Friederich, G., Matrai, P. A.,
894 Netcheva, S., Perovich, D. K., Santini, R., Shepson, P. B., Simpson, W., Valentic, T., Williams, C. and
895 Wyss, P. J.: Development of an autonomous sea ice tethered buoy for the study of ocean-atmosphere-sea
896 ice-snow pack interactions: The O-buoy, *Atmos. Meas. Tech.*, 3(1), 249–261, doi:10.5194/amt-3-249-
897 2010, 2010.
- 898 Koo, J. H., Wang, Y., Kurosu, T. P., Chance, K., Rozanov, A., Richter, A., Oltmans, S. J., Thompson, A.



- 899 M., Hair, J. W., Fenn, M. A., Weinheimer, A. J., Ryerson, T. B., Solberg, S., Huey, L. G., Liao, J., Dibb,
900 J. E., Neuman, J. A., Nowak, J. B., Pierce, R. B., Natarajan, M. and Al-Saadi, J.: Characteristics of
901 tropospheric ozone depletion events in the Arctic spring: Analysis of the ARCTAS, ARCPAC, and
902 ARCIONS measurements and satellite BrO observations, *Atmos. Chem. Phys.*, 12(20), 9909–9922,
903 doi:10.5194/acp-12-9909-2012, 2012.
- 904 Krnavek, L., Simpson, W. R., Carlson, D., Domine, F., Douglas, T. A. and Sturm, M.: The chemical
905 composition of surface snow in the Arctic: Examining marine, terrestrial, and atmospheric influences,
906 *Atmos. Environ.*, 50, 349–359, doi:10.1016/j.atmosenv.2011.11.033, 2012.
- 907 De Leeuw, G., Andreas, E. L., Anguelova, M. D., Fairall, C. W., Lewis, E. R., O’Dowd, C., Schulz, M.
908 and Schwartz, S. E.: Production flux of sea spray aerosol, *Rev. Geophys.*, 49(2), 1–39,
909 doi:10.1029/2010RG000349, 2011.
- 910 Lehrer, E., Hönninger, G. and Platt, U.: A one dimensional model study of the mechanism of halogen
911 liberation and vertical transport in the polar troposphere, *Atmos. Chem. Phys.*, 4(11/12), 2427–2440,
912 doi:10.5194/acp-4-2427-2004, 2004.
- 913 Lewis, E. R. and Schwartz, S. E.: Salt Aerosol Production: Mechanisms, Methods, Measurements, and
914 Models: A Critical Review, American Geophysical Union, Washington D.C., 2004.
- 915 Lin, H., Jacob, D. J., Lundgren, E. W., Sulprizio, M. P., Keller, C. A., Fritz, T. M., Eastham, S. D.,
916 Emmons, L. K., Campbell, P. C., Baker, B., Saylor, R. D. and Montuoro, R.: Harmonized Emissions
917 Component (HEMCO) 3.0 as a versatile emissions component for atmospheric models: Application in the
918 GEOS-Chem, NASA GEOS, WRF-GC, CESM2, NOAA GEFS-Aerosol, and NOAA UFS models,
919 *Geosci. Model Dev.*, 14(9), 5487–5506, doi:10.5194/gmd-14-5487-2021, 2021.
- 920 Liu, T., Chan, A. W. H. and Abbatt, J. P. D.: Multiphase Oxidation of Sulfur Dioxide in Aerosol
921 Particles: Implications for Sulfate Formation in Polluted Environments, *Environ. Sci. Technol.*,
922 *acs.est.0c06496*, doi:10.1021/acs.est.0c06496, 2021.
- 923 Mao, J., Paulot, F., Jacob, D. J., Cohen, R. C., Crouse, J. D., Wennberg, P. O., Keller, C. A., Hudman,
924 R. C., Barkley, M. P. and Horowitz, L. W.: Ozone and organic nitrates over the eastern United States:
925 Sensitivity to isoprene chemistry, *J. Geophys. Res. Atmos.*, 118(19), 11256–11268,
926 doi:10.1002/jgrd.50817, 2013.
- 927 Marelle, L., Thomas, J. L., Ahmed, S., Tuite, K., Stutz, J., Dommergue, A., Simpson, W. R., Frey, M. M.
928 and Baladima, F.: Implementation and Impacts of Surface and Blowing Snow Sources of Arctic Bromine
929 Activation Within WRF-Chem 4.1.1, *J. Adv. Model. Earth Syst.*, 13(8), doi:10.1029/2020ms002391,
930 2021.
- 931 McClure-Begley, A., Petropavlovskikh, I. and Oltmans, S.: NOAA Global Monitoring Surface Ozone
932 Network. 1973-2014. National Oceanic and Atmospheric Administration, Earth Systems Research
933 Laboratory Global Monitoring Division. Boulder, CO, , doi:10.7289/V57P8WBF, 2014.
- 934 Mcnamara, S. M., Kolesar, K. R., Wang, S., Kirpes, R. M., May, N. W., Gunsch, M. J., Cook, R. D.,
935 Fuentes, J. D., Hornbrook, R. S., Apel, E. C., Laskin, A. and Pratt, K. A.: Observation of Road Salt
936 Aerosol Driving Inland Wintertime Atmospheric Chlorine Chemistry, *ACS Cent. Sci.*, 6(684–694),
937 doi:10.1021/acscentsci.9b00994, 2020.
- 938 Moore, C. W., Obrist, D., Steffen, A., Staebler, R. M., Douglas, T. A., Richter, A. and Nghiem, S. V:
939 Convective forcing of mercury and ozone in the Arctic boundary layer induced by leads in sea ice.,
940 *Nature*, 506(7486), 81–4, doi:10.1038/nature12924, 2014.



- 941 NOAA ESRL Global Monitoring Division. 2018. Meteorology measurements from quasi-continuous 793
942 measurements at Barrow, Alaska, American Samoa and South Pole. Compiled by Christine Schultz. 794
943 National Oceanic and Atmospheric Administration (NOAA), Earth System Research Laboratory (ESRL),
944 795 Global Monitoring Division (GMD): Boulder, Colorado, USA.
- 945
- 946 Nghiem, S.: Studying bromine, ozone, and mercury chemistry in the Arctic, *Eos, Trans. Am. Geophys.*
947 *Union*, 94(33), 289–291, doi:10.1038/NGEO1779., 2013.
- 948 Oltmans, S. J., Johnson, B. J. and Harris, J. M.: Springtime boundary layer ozone depletion at Barrow,
949 Alaska: Meteorological influence, year-to-year variation, and long-term change, *J. Geophys. Res. Atmos.*,
950 117(8), 1–18, doi:10.1029/2011JD016889, 2012.
- 951 Oum, K. W., Lakin, M. J. and Finlayson-Pitts, B. J.: Bromine activation in the troposphere by the dark
952 reaction of O₃ with seawater ice, *Geophys. Res. Lett.*, 25(21), 3923–3926, doi:10.1029/1998GL900078,
953 1998.
- 954 Parrella, J. P., Jacob, D. J., Liang, Q., Zhang, Y., Mickley, L. J., Miller, B., Evans, M. J., Yang, X., Pyle,
955 J. A., Theys, N. and Van Roozendaal, M.: Tropospheric bromine chemistry: Implications for present and
956 pre-industrial ozone and mercury, *Atmos. Chem. Phys.*, 12(15), 6723–6740, doi:10.5194/acp-12-6723-
957 2012, 2012.
- 958 Payne, V. H., Clough, S. A., Shephard, M. W., Nassar, R. and Logan, J. A.: Information-centered
959 representation of retrievals with limited degrees of freedom for signal : Application to methane from the
960 Tropospheric Emission Spectrometer, *J. Geophys. Res.*, 114, 1–16, doi:10.1029/2008JD010155, 2009.
- 961 Peterson, P. K., Simpson, W. R., Pratt, K. A., Shepson, P. B., Frieß, U., Zielcke, J., Platt, U., Walsh, S. J.
962 and Nghiem, S. V.: Dependence of the vertical distribution of bromine monoxide in the lower troposphere
963 on meteorological factors such as wind speed and stability, *Atmos. Chem. Phys.*, 15, 2119–2137,
964 doi:10.5194/acp-15-2119-2015, 2015.
- 965 Peterson, P. K., Pöhler, D., Sihler, H., Zielcke, J., General, S., Frieß, U., Platt, U., Simpson, W. R.,
966 Nghiem, S. V., Shepson, P. B., Stirm, B. H., Dhaniyala, S., Wagner, T., Caulton, D. R., Fuentes, J. D. and
967 Pratt, K. A.: Observations of bromine monoxide transport in the Arctic sustained on aerosol particles,
968 *Atmos. Chem. Phys.*, 17(12), 7567–7579, doi:10.5194/acp-17-7567-2017, 2017.
- 969 Peterson, P. K., Pöhler, D., Zielcke, J., General, S., Friess, U., Platt, U., Simpson, W. R., Nghiem, S.,
970 Shepson, P. B., Stirm, B. H. and Pratt, K. A.: Springtime Bromine Activation Over Coastal and Inland
971 Arctic Snowpacks, *ACS Earth Sp. Chem.*, acsearthspacechem.8b00083,
972 doi:10.1021/acsearthspacechem.8b00083, 2018.
- 973 Peterson, P. K., Hartwig, M., May, N. W., Schwartz, E., Rigor, I., Ermold, W., Steele, M., Morison, J. H.,
974 Nghiem, S. V. and Pratt, K. A.: Snowpack measurements suggest role for multi-year sea ice regions in
975 Arctic atmospheric bromine and chlorine chemistry, *Elementa*, 2019.
- 976 Pöhler, D., Vogel, L., Friess, U. and Platt, U.: Observation of halogen species in the Amundsen Gulf,
977 Arctic, by active long-path differential optical absorption spectroscopy., *Proc. Natl. Acad. Sci. U. S. A.*,
978 107(15), 6582–7, doi:10.1073/pnas.0912231107, 2010.
- 979 Pound, R. J., Sherwen, T., Helmig, D., Carpenter, L. J. and Evans, M. J.: Influences of oceanic ozone
980 deposition on tropospheric photochemistry, *Atmos. Chem. Phys.*, 20(7), 4227–4239, doi:10.5194/acp-20-
981 4227-2020, 2020.
- 982 Pratt, K. A., Custard, K. D., Shepson, P. B., Douglas, T. A., Pöhler, D., General, S., Zielcke, J., Simpson,
983 W. R., Platt, U., Tanner, D. J., Gregory Huey, L., Carlsen, M. and Stirm, B. H.: Photochemical production
984 of molecular bromine in Arctic surface snowpacks, *Nat. Geosci.*, 6(5), 351–356, doi:10.1038/ngEO1779,



- 985 2013.
- 986 Richter, A., Wittrock, F., Eisinger, M. and Burrows, J. P.: GOME observations of tropospheric BrO in
987 Northern Hemispheric spring and summer 1997, *Geophys. Res. Lett.*, 25(14), 2683–2686,
988 doi:10.1029/98GL52016, 1998.
- 989 Rodgers, C. D. and Connor, B. J.: Intercomparison of remote sounding instruments, *J. Geophys. Res.*,
990 108(March 2002), doi:10.1029/2002JD002299, 2003.
- 991 Saiz-Lopez, A. and von Glasow, R.: Reactive halogen chemistry in the troposphere, *Chem. Soc. Rev.*,
992 41(19), 6448, doi:10.1039/c2cs35208g, 2012.
- 993 Salawitch, R. J., Canty, T., Kurosu, T., Chance, K., Liang, Q., Silva, A., Pawson, S., Nielsen, J. E.,
994 Rodriguez, J. M., Bhartia, P. K., Liu, X., Huey, L. G., Liao, J., Stickel, R. E., Tanner, D. J., Dibb, J. E.,
995 Simpson, W. R., Donohoue, D., Kreher, K., Johnston, P. V., Gao, R. S., Johnson, B., Bui, T. P. and Chen,
996 G.: A new interpretation of total column BrO during Arctic spring, *Geophys. Res. Lett.*, 37(21), 1–9,
997 doi:10.1029/2010GL043798, 2010.
- 998 Sander, R., Keene, W. C., Pszenny, A. A. P., Arimoto, R., Ayers, G. P., Baboukas, E., Caine, J. M.,
999 Crutzen, P. J., Duce, R. A., Hönninger, G., Huebert, B. J., Maenhaut, W., Mihalopoulos, N., Turekian, V.
1000 C. and Van Dingenen, R.: Inorganic bromine in the marine boundary layer: A critical review, *Atmos.*
1001 *Chem. Phys.*, 3(5), 1301–1336, doi:10.5194/acp-3-1301-2003, 2003.
- 1002 Schmidt, J. A., Jacob, D. J., Horowitz, H. M., Hu, L., Sherwen, T., Evans, M. J., Liang, Q., Suleiman, R.
1003 M., Oram, D. E., Le Breton, M., Percival, C. J., Wang, S., Dix, B. and Volkamer, R.: Modeling the
1004 observed tropospheric BrO background: Importance of multiphase chemistry and implications for ozone,
1005 OH, and mercury, *J. Geophys. Res.*, 121(19), 11819–11835, doi:10.1002/2015JD024229, 2016.
- 1006 Schroeder, W. H., Anlauf, K. G., Barrie, L. A., Lu, J. Y. and Steffen, A.: Arctic Springtime Depletion of
1007 Mercury, *Nature*, 394, 331–332, doi:10.1038/379126b0, 1998.
- 1008 Shah, V., Jacob, D. J., Moch, J. M., Wang, X. and Zhai, S.: Global modeling of cloud water acidity,
1009 precipitation acidity, and acid inputs to ecosystems, *Atmos. Chem. Phys.*, 12223–12245, 2020.
- 1010 Sherwen, T., Schmidt, J. A., Evans, M. J., Carpenter, L. J., Großmann, K., Eastham, S. D., Jacob, D. J., Dix,
1011 B., Koenig, T. K., Sinreich, R., Ortega, I., Volkamer, R., Saiz-Lopez, A., Prados-Roman, C., Mahajan, A.
1012 S. and C. Ordóñez: DISCUSS Global impacts of tropospheric halogens (Cl, Br, I) on oxidants and
1013 composition in GEOS-Chem, *Atmos. Chem. Phys. Discuss.*, (May), doi:10.5194/acp-2016-424, 2016a.
- 1014 Sherwen, T., Schmidt, J. A., Evans, M. J., Carpenter, L. J., Großmann, K., Eastham, S. D., Jacob, D. J.,
1015 Dix, B., Koenig, T. K., Sinreich, R., Ortega, I., Volkamer, R., Saiz-Lopez, A., Prados-Roman, C.,
1016 Mahajan, A. S. and Ordóñez, C.: Global impacts of tropospheric halogens (Cl, Br, I) on oxidants and
1017 composition in GEOS-Chem, *Atmos. Chem. Phys.*, 16(18), 12239–12271, doi:10.5194/acp-16-12239-
1018 2016, 2016b.
- 1019 Sherwen, T., Evans, M. J., Carpenter, L. J., Schmidt, J. A. and Mickely, L. J.: Halogen chemistry reduces
1020 tropospheric O₃ radiative forcing, *Atmos. Chem. Phys.*, (August), 1–18, doi:10.5194/acp-2016-688,
1021 2016c.
- 1022 Simpson, W. R.: Atmospheric measurements via Multiple Axis Differential Optical Absorption
1023 Spectroscopy (MAXDOAS), Utqiagvik (Barrow), Alaska 2012-2018. Arctic Data Center, Arcticdata.io,
1024 doi:10.18739/A2222R550, 2018.
- 1025 Simpson, W. R., Perovich, D. K., Matrai, P. A., Shepson, P. B. and Chavez, F.: The Collaborative O-
1026 Buoy Project: Deployment of a Network of Arctic Ocean Chemical Sensors for the IPY and beyond.
1027 Arctic Data Center, doi:10.18739/A2WD4W, 2009.



- 1028 Simpson, W. R., Brown, S. S., Saiz-Lopez, A., Thornton, J. A. and Glasow, R. Von: Tropospheric
1029 Halogen Chemistry: Sources, Cycling, and Impacts, *Chem. Rev.*, 150312153236002,
1030 doi:10.1021/cr5006638, 2015.
- 1031 Simpson, W. R., Peterson, P. K., Frieß, U., Sihler, H., Lampel, J., Platt, U., Moore, C., Pratt, K., Shepson,
1032 P., Halfacre, J. and Nghiem, S. V: Horizontal and vertical structure of reactive bromine events probed by
1033 bromine monoxide MAX-DOAS, *Atmos. Chem. Phys.*, 17, 9291–9309, 2017.
- 1034 Stutz, J., Thomas, J. L., Hurlock, S. C., Schneider, M., Von Glasow, R., Piot, M., Gorham, K., Burkhart,
1035 J. F., Ziemba, L., Dibb, J. E. and Lefer, B. L.: Longpath DOAS observations of surface BrO at Summit,
1036 Greenland, *Atmos. Chem. Phys.*, 11(18), 9899–9910, doi:10.5194/acp-11-9899-2011, 2011.
- 1037 Swanson, W. F., Graham, K. A., Halfacre, J. W., Holmes, C. D., Shepson, P. B. and Simpson, W. R.:
1038 Arctic Reactive Bromine Events Occur in Two Distinct Sets of Environmental Conditions : A Statistical
1039 Analysis of 6 Years of Observations *Journal of Geophysical Research : Atmospheres*, , 1–19,
1040 doi:10.1029/2019JD032139, 2020.
- 1041 Tang, T. and McConnell, J. C.: Autocatalytic release of bromine from Arctic snow pack during polar
1042 sunrise, *Geophys. Res. Lett.*, 23(19), 2633–2636, doi:10.1029/96GL02572, 1996.
- 1043 Theys, N., Van Roozendaal, M., Hendrick, F., Yang, X., De Smedt, I., Richter, A., Begoin, M., Errera,
1044 Q., Johnston, P. V., Kreher, K. and De Maziere, M.: Global observations of tropospheric BrO columns
1045 using GOME-2 satellite data, *Atmos. Chem. Phys.*, 11(4), 1791–1811, doi:10.5194/acp-11-1791-2011,
1046 2011.
- 1047 Thomas, J. L., Stutz, J., Lefer, B., Huey, L. G., Toyota, K., Dibb, J. E. and Von Glasow, R.: Modeling
1048 chemistry in and above snow at Summit, Greenland - Part 1: Model description and results, *Atmos.*
1049 *Chem. Phys.*, 11(10), 4899–4914, doi:10.5194/acp-11-4899-2011, 2011.
- 1050 Toom-Saunty, D. and Barrie, L. A.: Chemical composition of snowfall in the high Arctic: 1990-1994,
1051 *Atmos. Environ.*, 36(15–16), 2683–2693, doi:10.1016/S1352-2310(02)00115-2, 2002.
- 1052 Toyota, K., McConnell, J. C., Lupu, A., Neary, L., McLinden, C. A., Richter, A., Kwok, R., Semeniuk,
1053 K., Kaminski, J. W., Gong, S.-L., Jarosz, J., Chipperfield, M. P. and Sioris, C. E.: Analysis of reactive
1054 bromine production and ozone depletion in the Arctic boundary layer using 3-D simulations with GEM-
1055 AQ: inference from synoptic-scale patterns, *Atmos. Chem. Phys.*, 11(8), 3949–3979, doi:10.5194/acp-11-
1056 3949-2011, 2011.
- 1057 Toyota, K., Dastoor, A. P. and Ryzhkov, A.: Air-snowpack exchange of bromine, ozone and mercury in
1058 the springtime Arctic simulated by the 1-D model PHANTAS - Part 2: Mercury and its speciation,
1059 *Atmos. Chem. Phys.*, 14(8), 4135–4167, doi:10.5194/acp-14-4135-2014, 2014.
- 1060 Toyota, K., Dastoor, A. P. and Ryzhkov, A.: Parameterization of gaseous dry deposition in atmospheric
1061 chemistry models : Sensitivity to aerodynamic resistance formulations under statically stable conditions,
1062 *Atmos. Environ.*, 147, 409–422, doi:10.1016/j.atmosenv.2016.09.055, 2016.
- 1063 Travis, K. R., Jacob, D. J., Fisher, J. A., Kim, P. S., Marais, E. A., Zhu, L., Yu, K., Miller, C. C.,
1064 Yantosca, R. M., Sulprizio, M. P., Thompson, A. M., Wennberg, P. O., Crouse, J. D., St Clair, J. M.,
1065 Cohen, R. C., Laughner, J. L., Dibb, J. E., Hall, S. R., Ullmann, K., Wolfe, G. M., Pollack, I. B., Peischl,
1066 J., Neuman, J. A. and Zhou, X.: Why do models overestimate surface ozone in the Southeast United
1067 States?, *Atmos. Chem. Phys.*, 16(21), 13561–13577, doi:10.5194/acp-16-13561-2016, 2016.
- 1068 Vogt, R., Crutzen, P. and Sander, R.: A mechanism for halogen release from sea-salt, *Nature*,
1069 383(September), 327–331, 1996.
- 1070 Wagenbach, D., Minikin, A., Ducroz, F., Mulvaney, R., Keck, L., Legrand, M., Hall, J. S. and Wolff, E.



- 1071 W.: Sea-salt aerosol in coastal Antarctic regions at three coastal, *J. Geophys. Res. Atmos.*, 103, 961–974,
1072 1998.
- 1073 Wagner, T. and Platt, U.: Satellite mapping of enhanced BrO concentrations in the troposphere, *Nature*,
1074 395(October), 486–490, doi:10.1038/26723, 1998.
- 1075 Wang, S. and Pratt, K. A.: Molecular Halogens Above the Arctic Snowpack: Emissions, Diurnal
1076 Variations, and Recycling Mechanisms, *J. Geophys. Res. Atmos.*, 122(21), 11,991–12,007,
1077 doi:10.1002/2017JD027175, 2017.
- 1078 Wang, S., Mcnamara, S. M., Moore, C. W., Obrist, D., Steffen, A., Shepson, P. B., Staebler, R. M., Raso,
1079 A. R. W. and Pratt, K. A.: Direct detection of atmospheric atomic bromine leading to mercury and ozone
1080 depletion, *Proc. Natl. Acad. Sci.*, 116(29), doi:10.18739/A2D79598P.1, 2019a.
- 1081 Wang, X., Jacob, D. J., Eastham, S. D., Sulprizio, M. P., Zhu, L., Chen, Q., Alexander, B., Sherwen, T.,
1082 Evans, M. J., Lee, B. H., Haskins, J. D., Lopez-hilfiker, F. D., Thornton, J. A., Huey, G. L. and Liao, H.:
1083 The role of chlorine in global tropospheric chemistry, *Atmos. Chem. Phys.*, 3981–4003, 2019b.
- 1084 Wang, X., Jacob, D. J., Downs, W., Zhai, S., Zhu, L., Shah, V., Holmes, C. D., Sherwen, T., Alexander,
1085 B., Evans, M. J., Eastham, S. D., Neuman, J. A., Veres, P. R., Koenig, T. K., Volkamer, R., Huey, L. G.,
1086 Bannan, T. J., Percival, C. J., Lee, B. H. and Thornton, J. A.: Global tropospheric halogen (Cl, Br, I)
1087 chemistry and its impact on oxidants, *Atmos. Chem. Phys.*, 21(18), 13973–13996, doi:10.5194/acp-21-
1088 13973-2021, 2021.
- 1089 Wennberg, P. O.: Bromine explosion, *Nature*, 397(6717), 299–301, doi:10.1038/16805, 1999.
- 1090 Wren, S. N., Kahan, T. F., Jumaa, K. B. and Donaldson, D. J.: Spectroscopic studies of the heterogeneous
1091 reaction between O₃(g) and halides at the surface of frozen salt solutions, *J. Geophys. Res. Atmos.*,
1092 115(16), 1–8, doi:10.1029/2010JD013929, 2010.
- 1093 Wren, S. N., Donaldson, D. J. and Abbatt, J. P. D.: Photochemical chlorine and bromine activation from
1094 artificial saline snow, *Atmos. Chem. Phys.*, 13(19), 9789–9800, doi:10.5194/acp-13-9789-2013, 2013.
- 1095 Yang, X., Pyle, J. A. and Cox, R. A.: Sea salt aerosol production and bromine release: Role of snow on
1096 sea ice, *Geophys. Res. Lett.*, 35(16), 1–5, doi:10.1029/2008GL034536, 2008.
- 1097 Yang, X., Pyle, J. A., Cox, R. A., Theys, N. and Van Roozendaal, M.: Snow-sourced bromine and its
1098 implications for polar tropospheric ozone, *Atmos. Chem. Phys.*, 10(16), 7763–7773, doi:10.5194/acp-10-
1099 7763-2010, 2010.
- 1100 Yang, X., Frey, M., Rhodes, R., Norris, S., Brooks, I., Anderson, P., Nishimura, K., Jones, A. and Wolff,
1101 E.: Sea salt aerosol production via sublimating wind-blown saline snow particles over sea ice:
1102 parameterizations and relevant microphysical mechanisms, *Atmos. Chem. Phys.*, 19, 8407–8424, 2019.
- 1103 Zhu, L., Jacob, D. J., Eastham, S. D., Sulprizio, M. P., Wang, X., Sherwen, T., Evans, J., Chen, Q.,
1104 Alexander, B., Koenig, T. K., Volkamer, R. and Huey, L. G.: Effect of sea salt aerosol on tropospheric
1105 bromine chemistry, *Atmos. Chem. Phys.*, 6497–6507, 2019.
- 1106